Phonon-limited electron mobility in Si, GaAs, and GaP with exact treatment of dynamical quadrupoles

Guillaume Brunin [1], Henrique Pereira Coutada Miranda [1], Matteo Giantomassi [1], Miquel Royo [2], Massimiliano Stengel [2,3], Matthieu J. Verstraete [4,5], Xavier Gonze [1,6], Gian-Marco Rignanese [1], and Geoffroy Hautier [1,*]

[1]*UCLouvain, Institute of Condensed Matter and Nanosciences (IMCN), Chemin des Étoiles 8, B-1348 Louvain-la-Neuve, Belgium*
[2]*Institut de Ciència de Materials de Barcelona (ICMAB-CSIC), Campus UAB, 08193 Bellaterra, Spain*
[3]*ICREA-Institució Catalana de Recerca i Estudis Avançats, 08010 Barcelona, Spain*
[4]*NanoMat/Q-Mat/CESAM, Université de Liège (B5), B-4000 Liège, Belgium*
[5]*Catalan Institute of Nanoscience and Nanotechnology (ICN2), Campus UAB, 08193 Bellaterra, Spain*
[6]*Skolkovo Institute of Science and Technology, Skolkovo Innovation Center, Nobel St. 3, 143026, Moscow, Russia*

We describe a new approach to compute the electron-phonon self-energy and carrier mobilities in semiconductors. Our implementation does not require a localized basis set to interpolate the electron-phonon matrix elements, with the advantage that computations can be easily automated. Scattering potentials are interpolated on dense **q** meshes using Fourier transforms and *ab initio* models to describe the long-range potentials generated by dipoles and quadrupoles. To reduce significantly the computational cost, we take advantage of crystal symmetries and employ the linear tetrahedron method and double-grid integration schemes, in conjunction with filtering techniques in the Brillouin zone. We report results for the electron mobility in Si, GaAs, and GaP obtained with this new methodology.

I. INTRODUCTION

Electron-phonon (e-ph) interactions play an important role in various physical phenomena [1] such as conventional phonon-mediated superconductivity [2–7], phonon-assisted light absorption [8–10], temperature-dependent band structures, zero-point renormalization of the band gap in semiconductors [11–15], and thermal [16–18] and electrical conductivities [19–28]. Over the past years, several different open-source codes have been developed to compute e-ph related physical properties from first principles. For example, the e-ph self-energy (SE) and the renormalization of band energies can be obtained either with ABINIT [29–31] or YAMBO [32,33]. The latter relies on the e-ph matrix elements computed with QUANTUM ESPRESSO [34] and post-processes the data to compute the SE and quasiparticle corrections. With the EPW software [26,35], one can study several e-ph quantities using an interpolation scheme that exploits the localization in real space of the Wannier representation [36] to obtain the e-ph matrix elements in the full Brillouin zone (BZ) at a relatively small computational cost. Unfortunately the generation of maximally localized Wannier functions (MLWFs) is not always trivial and non-negligible effort may therefore be needed to obtain an appropriate set of MLWFs spanning the energy region of interest.[1] This is especially true

for systems whose band structure cannot be easily interpreted in terms of standard chemistry concepts, or when high-energy states must be included to compute the real part of the SE whose convergence with the number of empty states is notoriously slow [37]. It is therefore not surprising that recent works proposed to replace Wannier functions with atomic orbitals [38].

In this work, we present an alternative fully *ab initio* method to compute the e-ph SE using plane waves and Bloch wave functions as implemented in ABINIT [30,31,39] thus bypassing the transformation to localized orbitals. Particular emphasis is given to the calculation of the imaginary part of the SE and phonon-limited mobilities although a similar methodology can be employed for the real part of the SE and temperature-dependent band structures [1,11]. While our approach requires, in principle, more floating-point operations and more memory than a Wannier-based approach, it has the advantage that the computation can be automated with minimal input from the user and that systematic convergence studies can be easily performed. To make our approach competitive with Wannier-based implementations, we take full advantage of crystal symmetries and employ the linear tetrahedron method in conjunction with double-grid and filtering techniques both in **k** and **q** space. As a result, the number of e-ph matrix elements needed to reach convergence is significantly reduced. The scattering potentials are interpolated on arbitrary **q** grids using a Fourier-based interpolation scheme [40] in which the long-range dipolar and quadrupolar fields are treated using nonanalytic expressions depending on the high-frequency dielectric tensor, Born effective charges, dynamical quadrupoles tensors and the response to a homogeneous static electric field. The importance of the

---

*Corresponding author: geoffroy.hautier@uclouvain.be

[1]Considerable efforts have been made in recent years to develop more robust algorithms to localize Wannier orbitals using few tunable parameters. See, for example, the SCDM method proposed in Ref. [85].

dynamical quadrupoles for obtaining a reliable interpolation at small $\mathbf{q}$ is discussed in our accompanying letter [41]. Parallel scalability with memory distribution is achieved thanks to five different levels of MPI parallelism.

The paper is organized as follows. In Sec. II, we introduce the theory of e-ph interactions and its connection with state-of-the-art first-principles methods. We also provide more details on the Fourier interpolation of the scattering potentials and derive the expression for the long-range components including quadrupolar fields. In Sec. III, we lay out the formalism to compute phonon-limited transport properties, focusing on carrier mobilities within the linearized Boltzmann equation. The different strategies implemented to reduce the computational cost are discussed in Sec. IV. Finally, in Sec. V, we illustrate all these techniques by computing the phonon-limited mobility of electrons in Si, GaAs and GaP within the self-energy relaxation time approximation (SERTA). Atomic (Hartree) units are used throughout the paper.

II. ELECTRON-PHONON INTERACTION

In periodic solids, electron-phonon coupling effects are usually discussed in terms of the Hamiltonian [1,42]

$$\hat{H} = \hat{H}_\mathrm{e} + \hat{H}_\mathrm{ph} + \hat{H}_\text{e-ph}, \tag{1}$$

where

$$\hat{H}_\mathrm{e} = \sum_{n\mathbf{k}} \varepsilon_{n\mathbf{k}} \, \hat{c}^\dagger_{n\mathbf{k}} \hat{c}_{n\mathbf{k}} \tag{2}$$

describes noninteracting quasiparticles with crystalline momentum $\mathbf{k}$, band index n, and dispersion $\varepsilon_{n\mathbf{k}}$, while

$$\hat{H}_\mathrm{ph} = \sum_{\mathbf{q}\nu} \omega_{\mathbf{q}\nu} \left(\hat{a}^\dagger_{\mathbf{q}\nu} \hat{a}_{\mathbf{q}\nu} + \frac{1}{2} \right) \tag{3}$$

is the Hamiltonian associated to noninteracting phonons with wave vector $\mathbf{q}$, mode index ν and frequency $\omega_{\mathbf{q}\nu}$. $\hat{c}^\dagger_{n\mathbf{k}}$ and $\hat{c}_{n\mathbf{k}}$ ($\hat{a}^\dagger_{\mathbf{q}\nu}$ and $\hat{a}_{\mathbf{q}\nu}$) are fermionic (bosonic) creation and destruction operators. Finally,

$$\hat{H}_\text{e-ph} = \frac{1}{\sqrt{N_p}} \sum_{\substack{\mathbf{k},\mathbf{q} \\ mn\nu}} g_{mn\nu}(\mathbf{k}, \mathbf{q}) \, \hat{c}^\dagger_{m\mathbf{k}+\mathbf{q}} \hat{c}_{n\mathbf{k}} (\hat{a}_{\mathbf{q}\nu} + \hat{a}^\dagger_{-\mathbf{q}\nu}) \tag{4}$$

describes the coupling to first order in the atomic displacements, with N_p the number of unit cells in the Born-von Kármán supercell and $g_{mn\nu}(\mathbf{k}, \mathbf{q})$ the e-ph coupling matrix elements. In principle, Eq. (1) should include the so-called Debye-Waller (DW) Hamiltonian that gives the coupling to second-order in the atomic displacement [1,11]. This term contributes importantly to the real part of the SE and must therefore be included when computing quasiparticle corrections and temperature dependent band structures. In this work, however, we will be mainly focusing on the imaginary part of the e-ph SE hence the DW term will be ignored [1].

A. Connection with DFT and DFPT

The connection between the many-body Hamiltonian in Eq. (1) and density-functional theory (DFT) is established by using the Kohn-Sham (KS) band structure in Eq. (2) and phonons from density-functional perturbation theory (DFPT)

in Eq. (3) [1,43]. Finally, the e-ph matrix element, $g_{mn\nu}(\mathbf{k}, \mathbf{q})$, is computed using

$$g_{mn\nu}(\mathbf{k}, \mathbf{q}) = \langle \psi_{m\mathbf{k}+\mathbf{q}} | \, \Delta_{\mathbf{q}\nu} V^\mathrm{KS} | \psi_{n\mathbf{k}} \rangle, \tag{5}$$

where $\psi_{n\mathbf{k}}$ is the KS Bloch state and $\Delta_{\mathbf{q}\nu} V^\mathrm{KS}$ is the first-order variation of the self-consistent KS potential,

$$\Delta_{\mathbf{q}\nu} V^\mathrm{KS} = \frac{1}{\sqrt{2\omega_{\mathbf{q}\nu}}} \sum_{p\kappa\alpha} \frac{\partial V^\mathrm{KS}}{\partial \tau_{\kappa\alpha}} \frac{e_{\kappa\alpha,\nu}(\mathbf{q})}{\sqrt{M_\kappa}} \, e^{i\mathbf{q}\cdot\mathbf{R}_p} \tag{6}$$

where $e_{\kappa\alpha,\nu}(\mathbf{q})$ is the αth Cartesian component of the phonon eigenvector for the atom κ in the unit cell, M_κ its atomic mass, $\mathbf{R}_p$ are lattice vectors identifying the unit cell p, and $\boldsymbol{\tau}_\kappa$ the ion position in the unit cell. Following the convention of Ref. [1], we can write Eq. (6) in terms of a lattice-periodic function $\Delta_{\mathbf{q}\nu} v^\mathrm{KS}$ defined as

$$\Delta_{\mathbf{q}\nu} V^\mathrm{KS} = e^{i\mathbf{q}\cdot\mathbf{r}} \Delta_{\mathbf{q}\nu} v^\mathrm{KS}. \tag{7}$$

The latter can be obtained as

$$\Delta_{\mathbf{q}\nu} v^\mathrm{KS} = \frac{1}{\sqrt{2\omega_{\mathbf{q}\nu}}} \sum_{\kappa\alpha} \frac{e_{\kappa\alpha,\nu}(\mathbf{q})}{\sqrt{M_\kappa}} \, \partial_{\kappa\alpha,\mathbf{q}} v^\mathrm{KS}, \tag{8}$$

where

$$\partial_{\kappa\alpha,\mathbf{q}} v^\mathrm{KS} = \sum_p e^{-i\mathbf{q}\cdot(\mathbf{r}-\mathbf{R}_p)} \left. \frac{\partial V^\mathrm{KS}}{\partial \tau_{\kappa\alpha}} \right|_{(\mathbf{r}-\mathbf{R}_p)} \tag{9}$$

is the first-order derivative of the KS potential that can be obtained with DFPT by solving self-consistently a system of Sternheimer equations for a given $(\kappa\alpha, \mathbf{q})$ perturbation [44,45].

B. Interpolation of the e-ph matrix elements

Accurate calculations of e-ph properties require the coupling matrix elements on very dense $\mathbf{k}$- and $\mathbf{q}$-point grids. The explicit DFPT computation of $\partial_{\kappa\alpha,\mathbf{q}} v^\mathrm{KS}$ for many $\mathbf{q}$ points thus represents the main bottleneck of the entire process. To reduce the computational cost, following Ref. [40], we interpolate the scattering potentials in $\mathbf{q}$ space using Fourier transforms while the KS wave functions are obtained by performing a non-self-consistent (NSCF) calculation on arbitrary $\mathbf{k}$ meshes. In a pseudopotential-based implementation,[2] the KS potential is given by

$$V^\mathrm{KS}(\mathbf{r}, \mathbf{r}') = \underbrace{[V^\mathrm{H}[n](\mathbf{r}) + V^\mathrm{xc}[n](\mathbf{r}) + V^\mathrm{loc}(\mathbf{r})]}_{V^\mathrm{scf}(\mathbf{r})}$$
$$\times \, \delta(\mathbf{r} - \mathbf{r}') + V^\mathrm{nl}(\mathbf{r}, \mathbf{r}') \tag{10}$$

and consists of contributions from the Hartree part (V^H), the exchange-correlation (XC) potential (V^xc), and the bare pseudopotential term that, in turn, consists of the local (V^loc) and nonlocal (V^nl) parts [46]. Following the internal ABINIT convention, we group the Hartree, XC and local terms in a single potential, V^scf, although only the first two terms are computed self-consistently. The lattice-periodic part of the

---

[2]We assume norm-conserving pseudopotentials.

first-order derivative of the KS potential thus reads

$$\partial_{\kappa\alpha,\mathbf{q}}v^{\mathrm{KS}} = \underbrace{[\partial_{\kappa\alpha,\mathbf{q}}v^{\mathrm{H}} + \partial_{\kappa\alpha,\mathbf{q}}v^{\mathrm{xc}} + \partial_{\kappa\alpha,\mathbf{q}}v^{\mathrm{loc}}]}_{\partial_{\kappa\alpha,\mathbf{q}}v^{\mathrm{scf}}} + \partial_{\kappa\alpha,\mathbf{q}}v^{\mathrm{nl}}. \quad (11)$$

The real-space representation of $\partial_{\kappa\alpha,\mathbf{q}}v^{\mathrm{scf}}$ is obtained through the following Fourier transform:

$$W_{\kappa\alpha}(\mathbf{r} - \mathbf{R}_p) = \frac{1}{N_{\mathbf{q}}} \sum_{\mathbf{q}} e^{-i\mathbf{q}\cdot(\mathbf{R}_p-\mathbf{r})} \, \partial_{\kappa\alpha,\mathbf{q}}v^{\mathrm{scf}}(\mathbf{r}), \quad (12)$$

where the BZ sum is over the $N_{\mathbf{q}}$ $\mathbf{q}$ points of the initial grid employed in the DFPT calculation. $W_{\kappa\alpha}(\mathbf{r} - \mathbf{R}_p)$ represents the variation of the SCF potential associated with the displacement of the atom κ in the unit cell identified by $\mathbf{R}_p$ along the Cartesian direction α. Once $W_{\kappa\alpha}(\mathbf{r} - \mathbf{R}_p)$ is known, one can interpolate the potential at an arbitrary point $\tilde{\mathbf{q}}$ using the inverse Fourier transform:

$$\partial_{\kappa\alpha,\tilde{\mathbf{q}}}v^{\mathrm{scf}}(\mathbf{r}) \approx \sum_{\mathbf{R}_p} e^{i\tilde{\mathbf{q}}\cdot(\mathbf{R}_p-\mathbf{r})} W_{\kappa\alpha}(\mathbf{r} - \mathbf{R}_p), \quad (13)$$

where the sum is over the real-space lattice vectors in the supercell associated to the $\mathbf{q}$ mesh used in Eq. (12). Note that only the SCF part of the DFPT potential needs to be interpolated as the derivative on the nonlocal part V^{nl} can be computed analytically [44].

Our approach therefore differs from Wannier-based methods in which electrons and phonons are treated on the same footing and the e-ph vertex is expressed in real space as a two-point function [47]. The advantage of our method is that the Wannierization step is completely avoided since the electronic wave functions are treated exactly and only phonon-related quantities (scattering potentials, phonon eigenvectors and frequencies) need to be interpolated. The price to pay is that one must perform an explicit NSCF calculation of the Bloch states on the dense $\mathbf{k}$ mesh and the computation of the e-ph matrix elements [Eq. (5)] now requires the application of the first order KS Hamiltonian. It should be noted, however, that the NSCF part represents a small fraction of the overall computing time when compared to the DFPT calculations that must be performed for each $\mathbf{q}$ point in the IBZ and all irreducible atomic perturbations. The application of the first order Hamiltonian is floating-point intensive but one can benefit from highly efficient fast Fourier transforms to apply $\partial_{\kappa\alpha,\mathbf{q}}v^{\mathrm{scf}}$ in $\mathbf{r}$ space while the derivative of the nonlocal part is computed directly in $\mathbf{G}$ space using pseudopotentials in the fully separable Kleinman-Bylander form [48]. In Sec. IV C, we also explain how to take advantage of homogeneous BZ meshes and filtering techniques to reduce considerably the number of matrix elements that must be computed.

C. Long-wavelength limit in semiconductors

The accuracy of the interpolation in Eq. (13) depends on the density of the initial *ab initio* $\mathbf{q}$ mesh that in turn defines the size of the Born–von Kármán supercell. This technique was initially proposed to study superconducting properties in metals and initial $\mathbf{q}$ meshes of the order of $8 \times 8 \times 8$ were found sufficient to obtain accurate results [40]. In metals, indeed, the screened potential is usually short ranged provided one excludes pathological cases associated to Kohn

anomalies [49]. In semiconductors, on the contrary, the long-range (LR) behavior of the screened potential is associated to nonanalyticities for $\mathbf{q} \to \mathbf{0}$ that must be avoided in the Fourier interpolation, and thus be handled separately.

We now generalize the standard technique used in polar semiconductors to cope with these LR nonanalytic contributions to the scattering potentials, and analyze in detail the contribution of quadrupolar terms. We recover the formal study done by Vogl in 1976 [50] in the context of many-body perturbation theory (MBPT), and update it to the DFPT treatment of atomic displacement and electric field response [44], as currently implemented in ABINIT and other first-principles packages. We also establish the connection with the treatment of Born effective charges and dynamical quadrupoles by Stengel [51]. Finally, we show how the nonanalytic terms are treated in the relevant interpolations, as already done for the lowest-order dipole-dipole nonanalytic contribution to the interatomic force constants [44] and for the Fröhlich-type dipole-induced scattering potential [52], both relying on the Born effective charges. We extend the latter work to the next order by including dynamical quadrupoles and local-field potentials.

For this purpose, the nonanalytic long-wavelength components ($\mathbf{q} \to \mathbf{0}$) of the first-order derivative of the SCF potential $\partial_{\kappa\alpha,\mathbf{q}}v^{\mathrm{scf}}(\mathbf{r})$ must be identified. Our aim is to retain all contributions that are $\mathcal{O}(q_{\alpha}/q^2)$ with q the norm of $\mathbf{q}$ (the strongest divergence is dipole-like and has already been treated, e.g., in Ref. [52]), as well as $\mathcal{O}(q_{\alpha}q_{\beta}/q^2)$, linked to quadrupoles and local field potentials with nonanalytic directional behavior, as shown in the following. On the other hand, we will neglect all $\mathcal{O}(q_{\alpha}q_{\beta}q_{\gamma}/q^2)$ contributions (associated with octupoles) and analytic $\mathcal{O}(1)$ contributions that can already be Fourier interpolated. We will obtain the above-mentioned behaviors after alignment and rescaling of the wave-vector components. In the following, for a real-space function $f_{\mathbf{q}}(\mathbf{r})$, we denote generically with $f_{\mathbf{q}}(\mathbf{G})$ the components of its Fourier decomposition:

$$f_{\mathbf{q}}(\mathbf{r}) = \sum_{\mathbf{G}} f_{\mathbf{q}}(\mathbf{G}) e^{i(\mathbf{q}+\mathbf{G})\cdot\mathbf{r}}. \quad (14)$$

Let us first focus on the $\mathbf{q} \to \mathbf{0}$ behavior of the first-order derivatives of the wave functions with respect to collective atomic displacements, $|u_{n\mathbf{k},\mathbf{q}\to\mathbf{0}}^{\tau_{\kappa\alpha}}\rangle$ [15,51]. The computation of these quantities implies auxiliary DFPT calculations, delivering $|u_{n\mathbf{k},\mathbf{q}=\mathbf{0}}^{\tau'_{\kappa\alpha}}\rangle$ and $|u_{n\mathbf{k}}^{\mathcal{E}'_\lambda}\rangle$. These are obtained by considering perturbations of the collective atomic displacement and of the electric field types, at $\mathbf{q} = \mathbf{0}$, in which the divergent $\mathbf{G} = \mathbf{0}$ component of the first-order derivative of the Hartree potential $\frac{4\pi}{q^2}$ has been removed, see Eq. (A2). From Ref. [15], we can express the derivatives of the wave functions *with* the $\mathbf{G} = \mathbf{0}$ contribution to the Hartree potential as

$$|u_{n\mathbf{k},\mathbf{q}\to\mathbf{0}}^{\tau_{\kappa\alpha}}\rangle = |u_{n\mathbf{k},\mathbf{q}=\mathbf{0}}^{\tau'_{\kappa\alpha}}\rangle + \frac{4\pi}{\Omega} \frac{(-\mathcal{Q})(q_{\gamma}Z_{\kappa\alpha,\gamma}^*)q_{\lambda}|u_{n\mathbf{k}}^{\mathcal{E}'_\lambda}\rangle}{q^2\epsilon_M(\mathbf{q})} e^{-iq_\eta\tau_{\kappa\eta}}, \quad (15)$$

where $\epsilon_M(\mathbf{q})$ is the $\mathbf{q}$-dependent macroscopic dielectric function, $\mathbf{Z}_\kappa^*$ is the Born effective charge tensor, η, γ and λ, are Cartesian coordinates, and $\mathcal{Q}$ is the electronic charge in atomic

units, that is, -1. The sum over repeated indices is implied in this equation and in the remaining of this section. See Appendix A for more details about the derivation of Eq. (15).

We now generalize Eq. (15) to arbitrary $\mathbf{q}$ wave vectors. We consider a first auxiliary DFPT calculation with respect to collective atomic displacements, now at nonzero $\mathbf{q}$, where the $\mathbf{G} = \mathbf{0}$ component of the first-order derivative of the Hartree potential has been removed, delivering $|u_{n\mathbf{k},\mathbf{q}}^{\tau'_{\kappa\alpha}}\rangle$. The second auxiliary DFPT calculation is with respect to a monochromatic scalar potential ϕ, with nonzero $\mathbf{q}$, as defined in Ref. [53], again without the $\mathbf{G} = \mathbf{0}$ contribution to the first-order derivative of the Hartree potential. The corresponding first-order wave function is $|u_{n\mathbf{k},\mathbf{q}}^{\phi'}\rangle$. The first-order DFPT response of the wave functions to collective atomic displacements, at nonzero $\mathbf{q}$ *with* the $\mathbf{G} = \mathbf{0}$ contribution to the Hartree potential is then obtained as

$$|u_{n\mathbf{k},\mathbf{q}}^{\tau_{\kappa\alpha}}\rangle = |u_{n\mathbf{k},\mathbf{q}}^{\tau'_{\kappa\alpha}}\rangle + \frac{4\pi}{\Omega}\frac{\mathcal{Q}Q_{\kappa\alpha}^{\mathbf{q}}}{q^2\epsilon_M(\mathbf{q})}|u_{n\mathbf{k},\mathbf{q}}^{\phi'}\rangle e^{-iq_\eta\tau_{\kappa\eta}}, \quad (16)$$

see Appendix A for more details. In the long-wavelength limit, the cell-integrated charge response to a monochromatic atomic displacement $Q_{\kappa\alpha}^{\mathbf{q}}$ is [53]

$$Q_{\kappa\alpha}^{\mathbf{q}} = -iq_\gamma Z_{\kappa\alpha,\gamma}^* - \frac{q_\beta q_\gamma}{2}Q_{\kappa\alpha}^{\beta\gamma} + \cdots, \quad (17)$$

where $Q_{\kappa\alpha}^{\beta\gamma}$ is the dynamical quadrupole.

The self-consistency loop is linear in the first-order derivatives of the different quantities that are connected through it. So, the first-order change of the density, the first-order derivatives of the SCF and Kohn-Sham potentials of the $\tau_{\kappa\alpha}$ perturbation bear the same relation to those of the $\tau'_{\kappa\alpha}$ and ϕ' perturbation, than the one obtained for the wave functions, Eq. (16). For the phase-factorized periodic part of the KS potential [see Eqs. (7)–(9)], we obtain

$$\partial_{\kappa\alpha,\mathbf{q}}v^{\mathrm{KS}} = \partial'_{\kappa\alpha,\mathbf{q}}v^{\mathrm{KS}} + \frac{4\pi}{\Omega}\frac{Q_{\kappa\alpha}^{\mathbf{q}}}{q^2\epsilon_M(\mathbf{q})}\big(1 + \mathcal{Q}\partial'_\phi v_{\mathbf{q}}^{\mathrm{Hxc}}\big)e^{-iq_\eta\tau_{\kappa\eta}}, \quad (18)$$

where the prime refers again to the auxiliary DFPT calculations and we have taken into account that the ϕ perturbation has an external scalar $\mathcal{Q}$ contribution and that the nonlocal term is not present in the ϕ perturbation or in the corresponding Hartree or XC potentials. This formula allows one to compute the e-ph matrix elements in the vicinity of $\mathbf{q} = \mathbf{0}$, to all orders in q.

We can now derive the dipole and quadrupole-type non-analyticities through the analysis of the different contributing terms. The first term in Eq. (18) is analytic. The denominator of the second term, $q^2\epsilon_M(\mathbf{q})$, expands as [15]

$$q^2\epsilon_M(\mathbf{q}) = q_\delta\epsilon_{\delta\delta'}^\infty q_{\delta'} + \mathcal{O}(q^4), \quad (19)$$

where $\boldsymbol{\epsilon}^\infty$ is the high-frequency dielectric tensor. Appearing in the denominator, it gives the nonanalytic behavior of the second term. There is no cubic contribution in q in this expansion, as emphasized by Vogl [50]. The $\boldsymbol{\epsilon}^\infty$ tensor might be used as a metric, to highlight the $\mathcal{O}(q^2)$ character of this denominator [44].

Equation (17) shows that the expansion of $Q_{\kappa\alpha}^{\mathbf{q}}$ is analytic, and likewise for $\partial'_\phi v^{\mathrm{Hxc}}$, whose expansion starts with the term proportional to q:

$$\partial'_\phi v_{\mathbf{q}}^{\mathrm{Hxc}} = iq_\alpha v^{\mathrm{Hxc},\mathcal{E}_\alpha} + \mathcal{O}(q^2). \quad (20)$$

Thus the dominant nonanalyticity is a real-space constant shift in the potential, of dipolar character (i.e., of order $\frac{q_\alpha}{q^2}$ considering the appropriate metric in reciprocal space):

$$\frac{4\pi}{\Omega}\frac{iq_\gamma Z_{\kappa\alpha,\gamma}^*}{q_\delta\epsilon_{\delta\delta'}^\infty q_{\delta'}}e^{-iq_\eta\tau_{\kappa\eta}}. \quad (21)$$

At the quadrupole level (i.e., of order $\frac{q_\beta q_\gamma}{q^2}$ in the proper metric), there are two contributions: a real-space constant shift,

$$\frac{4\pi}{\Omega}\frac{\big(\frac{q_\beta q_\gamma}{2}\big)Q_{\kappa\alpha}^{\beta\gamma}}{q_\delta\epsilon_{\delta\delta'}^\infty q_{\delta'}}e^{-iq_\eta\tau_{\kappa\eta}}, \quad (22)$$

and a nonconstant real-space potential,

$$\frac{4\pi}{\Omega}\frac{(-q_\beta q_\gamma)Z_{\kappa\alpha,\beta}^*}{q_\delta\epsilon_{\delta\delta'}^\infty q_{\delta'}}\mathcal{Q}v^{\mathrm{Hxc},\mathcal{E}_\gamma}(\mathbf{r})e^{-iq_\eta\tau_{\kappa\eta}}. \quad (23)$$

The latter is obtained from ABINIT, considering the electric field ($\mathcal{Q}\mathcal{E}_\alpha$) perturbation.

These terms parallel those found in the MBPT context by Vogl [50]. Note, however, that Vogl was focusing on the e-ph scattering matrix elements for some well-defined normal mode of vibration while the present work focuses on the collective displacement of a given single sublattice κ in a specific direction α. In this context, Vogl obtained a third quadrupole contribution that is not present here. The generalization of Eq. (21) to finite $\mathbf{G}$ has already been done in Ref. [52]. The generalization of Eqs. (22) and (23) follows the same derivation. The expression for the LR model finally reads

$$V_{\kappa\alpha,\mathbf{q}}^{\mathcal{L}}(\mathbf{r}) = \frac{4\pi}{\Omega}\sum_{\mathbf{G}\neq-\mathbf{q}}\frac{i(q_\beta+G_\beta)Z_{\kappa\alpha,\beta}^* - (q_\beta+G_\beta)(q_\gamma+G_\gamma)\big(Z_{\kappa\alpha,\beta}^*\mathcal{Q}v^{\mathrm{Hxc},\mathcal{E}_\gamma}(\mathbf{r}) - \frac{1}{2}Q_{\kappa\alpha}^{\beta\gamma}\big)}{(q_\delta+G_\delta)\epsilon_{\delta\delta'}^\infty(q_{\delta'}+G_{\delta'})}e^{i(q_\eta+G_\eta)(r_\eta-\tau_{\kappa\eta})}. \quad (24)$$

In the actual implementation, following previous approaches [1,54], each component is multiplied by the Gaussian filter $e^{-\frac{|\mathbf{q}+\mathbf{G}|^2}{4\alpha}}$.[3]

---

[3]The α parameter determines the separation between the long-range and the short-range parts of the interaction and is used to express Ewald sums [44,86] in terms of a sum in $\mathbf{G}$ space (long-range part) and a sum in real space that, being short ranged, is not relevant for the definition of the LR model. The optimal value of α is material-dependent and should therefore be subject to convergence studies. In our systems, we observed small changes in the physical observables ($\sim$1%) with α. A value of 0.1 Bohr^{-2} is used in all calculations.

The impact of the electric-field term in Eq. (24) has been analyzed in details in Ref. [41]. In Si, GaP, and GaAs, the effect of the $\mathcal{E}$ term on the Fourier interpolation is negligible compared to the role played by $Q_{\kappa\alpha}^{\beta\gamma}$. Therefore we do not include the $\mathcal{E}$ term in the computations reported in this work. We do treat, however, the dipole-quadrupole and quadrupole-quadrupole interactions when interpolating the phonon frequencies following the formalism detailed in Ref. [51].

III. PHONON-LIMITED TRANSPORT PROPERTIES

A. Electron lifetimes

The electron lifetime due to the e-ph scattering is related to the inverse of the imaginary part of the e-ph Fan-Migdal SE [1]. The diagonal matrix elements of the SE in the KS basis set are given by

$$
\Sigma_{n\mathbf{k}}^{\mathrm{FM}}(\omega, \varepsilon_F, T) = \sum_{m,\nu} \int_{\mathrm{BZ}} \frac{d\mathbf{q}}{\Omega_{\mathrm{BZ}}} |g_{mn\nu}(\mathbf{k}, \mathbf{q})|^2
$$
$$
\times \left[\frac{n_{\mathbf{q}\nu}(T) + f_{m\mathbf{k}+\mathbf{q}}(\varepsilon_F, T)}{\omega - \varepsilon_{m\mathbf{k}+\mathbf{q}} + \omega_{\mathbf{q}\nu} + i\eta} \right.
$$
$$
\left. + \frac{n_{\mathbf{q}\nu}(T) + 1 - f_{m\mathbf{k}+\mathbf{q}}(\varepsilon_F, T)}{\omega - \varepsilon_{m\mathbf{k}+\mathbf{q}} - \omega_{\mathbf{q}\nu} + i\eta} \right], \quad (25)
$$

where $f_{m\mathbf{k}+\mathbf{q}}(\varepsilon_F, T)$ and $n_{\mathbf{q}\nu}(T)$ correspond to the Fermi-Dirac and Bose-Einstein occupation functions with T the temperature and ε_F the Fermi level. For the sake of simplicity, the temperature and Fermi level are considered as parameters, and the dependence on T and ε_F will be omitted in the following. The integral in Eq. (25) is performed over the $\mathbf{q}$ points in the BZ of volume Ω_{BZ} and η is a positive real infinitesimal.

In the $\eta \to 0^+$ limit, the imaginary part of the SE [Eq. (25)] evaluated at the KS energy is given by [1]

$$
\lim_{\eta \to 0^+} \Im\left\{ \Sigma_{n\mathbf{k}}^{\mathrm{FM}}(\varepsilon_{n\mathbf{k}}) \right\}
$$
$$
= \pi \sum_{m,\nu} \int_{\mathrm{BZ}} \frac{d\mathbf{q}}{\Omega_{\mathrm{BZ}}} |g_{mn\nu}(\mathbf{k}, \mathbf{q})|^2
$$
$$
\times [(n_{\mathbf{q}\nu} + f_{m\mathbf{k}+\mathbf{q}})\delta(\varepsilon_{n\mathbf{k}} - \varepsilon_{m\mathbf{k}+\mathbf{q}} + \omega_{\mathbf{q}\nu})
$$
$$
+ (n_{\mathbf{q}\nu} + 1 - f_{m\mathbf{k}+\mathbf{q}})\delta(\varepsilon_{n\mathbf{k}} - \varepsilon_{m\mathbf{k}+\mathbf{q}} - \omega_{\mathbf{q}\nu})] \quad (26)
$$

and corresponds to the linewidth of the electron state $n\mathbf{k}$ due to the scattering with phonons. Finally, the electron lifetime $\tau_{n\mathbf{k}}$ is inversely proportional to the linewidth of the SE evaluated at the KS energy [26,35]:

$$
\frac{1}{\tau_{n\mathbf{k}}} = 2 \lim_{\eta \to 0^+} \Im\left\{ \Sigma_{n\mathbf{k}}^{\mathrm{FM}}(\varepsilon_{n\mathbf{k}}) \right\}. \quad (27)
$$

These lifetimes play an important role in different physical properties, such as optical absorption [55] or transport properties [56]. In this work, we focus on the accurate computation of phonon-induced lifetimes and transport properties, without taking into account other scattering processes due to defects, impurities, grain boundaries or other electrons. As we include only one of the possible scattering mechanisms, our computed

mobilities are expected to overestimate the experimental results.[4]

B. Carrier mobility

In this article, we focus on the solution of the linearized Boltzmann transport formulation [57] within the relaxation time approximation (RTA). The generalized transport coefficients are given by [56]

$$
\mathcal{L}_{\alpha\beta}^{(m)} = -\sum_n \int \frac{d\mathbf{k}}{\Omega_{\mathrm{BZ}}} v_{n\mathbf{k},\alpha} v_{n\mathbf{k},\beta}\, \tau_{n\mathbf{k}} (\varepsilon_{n\mathbf{k}} - \varepsilon_F)^m \left. \frac{\partial f}{\partial \varepsilon} \right|_{\varepsilon_{n\mathbf{k}}} \quad (28)
$$

where $v_{n\mathbf{k},\alpha}$ is the α-th component of the matrix element $\mathbf{v}_{n\mathbf{k}}$ of the electron velocity operator. These quantities can be obtained from interpolation methods such as Wannier [58] or Shankland-Koelling-Wood (SKW) [59–62] whose form allows one to analytically compute the derivatives of the eigenvalues with respect to $\mathbf{k}$. Alternatively, one can obtain $\mathbf{v}_{n\mathbf{k}}$ using finite differences between shifted grids [55]. In our implementation, we prefer to compute the velocity matrix elements without any approximation using the commutator of the Hamiltonian with the position operator [63]:

$$
\mathbf{v}_{n\mathbf{k}} = \frac{\partial \varepsilon_{n\mathbf{k}}}{\partial \mathbf{k}} = \langle \psi_{n\mathbf{k}} | \hat{\mathbf{p}} + i [V^{\mathrm{nl}}, \mathbf{r}] | \psi_{n\mathbf{k}} \rangle \quad (29)
$$

with $\hat{\mathbf{p}}$ the momentum operator, as done in DFPT calculations of the response to an external electric field [44]. We note, in passing, that the group velocities can be used to compute transport lifetimes within the so-called momentum relaxation time approximation [22,23].

The generalized transport coefficients can be used to obtain different transport properties such as the electrical conductivity, Peltier and Seebeck coefficients, and charge carrier contribution to the thermal conductivity tensors [56]. The electrical conductivity tensor is given by

$$
\sigma_{\alpha\beta} = \frac{1}{\Omega} \mathcal{L}_{\alpha\beta}^{(0)} \quad (30)
$$

and can be divided into hole and electron contributions:[5]

$$
\sigma = n_e \mu_e + n_h \mu_h \quad (31)
$$

where n_e and n_h are the electron and hole concentrations in the conduction and valence bands respectively, and μ_e and μ_h are the electron and hole mobilities, which can be obtained by selecting the conduction or valences states n in Eq. (28). For electrons,

$$
n_e = \sum_{n \in \mathrm{CB}} \int \frac{d\mathbf{k}}{\Omega_{\mathrm{BZ}}} f_{n\mathbf{k}}, \quad \mu_e = \frac{1}{n_e \Omega} \mathcal{L}_{n \in \mathrm{CB}}^{(0)} \quad (32)
$$

where $n \in \mathrm{CB}$ denotes states in the conduction bands. Similar expressions hold for holes. At zero total carrier concentration,

---

[4]Scattering by defects, impurities, grain boundaries, or other electrons can be described either using semi-empirical models [66,87] or first-principles computations [20,88]. The computation of these effects is however outside the scope of the present work.

[5]We consider the conductivity related to the electric field only, not the Hall mobility [77].

the Fermi level ε_F is located inside the band gap so that $n_e = n_h$.

The transport coefficients in Eq. (28) depend both on the temperature and the doping level (through ε_F). Formally, $\tau_{n\mathbf{k}}$ also depends on ε_F through the Fermi-Dirac occupations in Eq. (26). A commonly used approximation consists in neglecting the variation of $\tau_{n\mathbf{k}}$ with ε_F. Under this assumption, Eq. (28) can be solved for different ε_F at almost no additional cost. This approach is valid when the transport coefficients are obtained for values of ε_F similar to the ones used to compute $\tau_{n\mathbf{k}}$.

IV. EFFICIENT COMPUTATION OF E-PH QUANTITIES

A. Use of symmetries

As mentioned in the introduction, our implementation exploits crystal symmetries to reduce the computational cost and the memory requirements. As concerns the KS wave functions, the NSCF calculation can be restricted to the $\mathbf{k}$ points in the IBZ of the unperturbed system as the Bloch states in the full BZ can be reconstructed by symmetry using the equations given in Appendix B. At the level of the scattering potentials, the DFPT computations need to be performed only for $\mathbf{q}$ points in the IBZ and, for each $\mathbf{q}$ point, only an appropriate set of irreducible perturbations needs to be computed explicitly. As shown in Appendix C, all the scattering potentials can be reconstructed from this irreducible set. These symmetry properties are used, for instance, to compute the sum over $\mathbf{q}$ points in the full BZ in Eq. (12).

Symmetries are also used in the computation of the electron lifetimes. First of all, the SE operator is invariant under the action of all the operations of the space group of the crystal. As a consequence, the computation of $\tau_{n\mathbf{k}}$ can be restricted to the $\mathbf{k}$ points in IBZ as $\tau_{n\mathbf{k}}$ transforms as the KS eigenvalues $\varepsilon_{n\mathbf{k}}$. Last but not least, for a given $\mathbf{k}$ point, the integral in $\mathbf{q}$ space in Eq. (26) can be restricted to an appropriate irreducible wedge (IBZ$_\mathbf{k}$) defined by the operations of the little group of $\mathbf{k}$, i.e., the set of point group operations that leave the $\mathbf{k}$-point invariant modulo a reciprocal lattice vector $\mathbf{G}$.

B. Tetrahedron method

The evaluation of Eq. (26) requires an accurate integration of the Dirac δ distribution, especially in the regions around the band edges where lifetimes usually show strong variations and anisotropic behavior. For practical applications, it is customary to replace the δ distribution by Lorentzian or Gaussian functions with a small but finite width, also called the broadening parameter η. According to previous studies [28], Gaussian functions lead to a faster convergence of the $\mathbf{q}$-point integral in Eq. (26). From a theoretical perspective, the use of Lorentzian functions is more appropriate because, in Eq. (25), the δ distribution is obtained as the limit of a Lorentzian for $\eta \to 0$. It should be stressed, however, that both the Lorentzian and Gaussian methods require careful convergence studies: for a given value of η, physical quantities should be converged by increasing the density of $\mathbf{q}$ points then one should monitor the behavior of the converged values for $\eta \to 0$ and select a broadening for which the results are relatively stable.
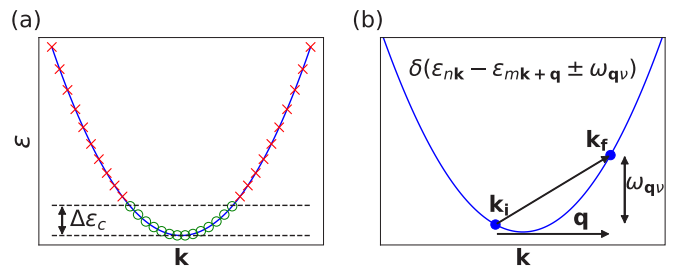

FIG. 1. Schematic representation of the filtering of (a) $\mathbf{k}$ and (b) $\mathbf{q}$ points for the computation of the SE in the case of a single parabolic conduction band at the Γ point. (a) States represented by green dots (red crosses) are included (excluded) in (from) the transport computation according to the input variable $\Delta\varepsilon_c$. (b) For initial and final electron states $\mathbf{k_i}$ and $\mathbf{k_f}$, the wave vector $\mathbf{q} = \mathbf{k_f} - \mathbf{k_i}$ requires a phonon mode with frequency $\omega_{\mathbf{q}\nu} = \varepsilon_{\mathbf{k_f}} - \varepsilon_{\mathbf{k_i}}$. If this condition is not fulfilled, the $\mathbf{q}$ point is ignored.

To avoid this additional convergence study, we prefer to compute Eq. (26) with the linear tetrahedron method. The implementation closely follows the algorithm proposed by Blöchl [64]. The full BZ is first partitioned into tetrahedra, then symmetries are used to identify a set of irreducible tetrahedra with the corresponding corners and multiplicity. The presence of $\varepsilon_{m\mathbf{k}+\mathbf{q}}$ in the argument of the two δ functions implies that only the symmetries of the little group of $\mathbf{k}$ can be used to define the irreducible tetrahedra covering the IBZ$_\mathbf{k}$. Once the irreducible tetrahedra have been identified for a given $\mathbf{k}$, the squared modulus of the e-ph matrix element as well as the $F_{m\nu}^{\pm}(\mathbf{q}) = \varepsilon_{m\mathbf{k}+\mathbf{q}} \pm \omega_{\mathbf{q}\nu}$ functions are linearly interpolated in $\mathbf{q}$ space using the values at the corners of each tetrahedron. Within the linear approximation, the isosurfaces $F_{m\nu}^{\pm}(\mathbf{q}) = \varepsilon_{n\mathbf{k}}$ become planes that may cut the tetrahedron depending on the value of $\varepsilon_{n\mathbf{k}}$ and the integration inside each tetrahedron is performed analytically. Finally, as discussed in Ref. [64], the sum over tetrahedra is converted into a weighted sum over the $\mathbf{q}$ points in the IBZ$_\mathbf{k}$ with different weights $w^{\pm}(n, m, \nu, \mathbf{q})$ for absorption and emission processes. The weights are nonzero only for $\mathbf{q}$ points associated to tetrahedra intersecting one of the possible isosurfaces. This is the key to the filtering algorithm in $\mathbf{q}$ space discussed in more details in the next section.

C. k- and q points filtering

An initial filtering is achieved by noticing that the derivative of the Fermi occupation f in Eq. (28) is practically nonzero only for electronic states close to the Fermi level. Since ε_F is usually inside the band gap, only electronic states with $\mathbf{k}$ and $\varepsilon_{n\mathbf{k}}$ close to the band edge(s) contribute to Eq. (28) [65]. In our implementation, we use an input variable that defines the energy range for electrons ($\Delta\varepsilon_c$) and holes ($\Delta\varepsilon_v$): if $\varepsilon_{n\mathbf{k}} - \varepsilon_{\mathrm{CBM}} > \Delta\varepsilon_v$ or $\varepsilon_{\mathrm{VBM}} - \varepsilon_{n\mathbf{k}} > \Delta\varepsilon_v$, the lifetime $\tau_{n\mathbf{k}}$ is not computed because this state is assumed to give negligible contribution to Eq. (28). This selection algorithm is depicted in Fig. 1(a), where $\tau_{n\mathbf{k}}$ is computed for the states represented by green circles but not for the red crosses.

The achievable speedup depends on the band dispersion, the position of the Fermi level and the temperature. In most cases, the effective number of **k** points is much smaller than the initial number of wave vectors in the IBZ associated to the homogeneous mesh. In Sec. V C, it is shown that converged electron mobilities in Si and GaP can be obtained with around 29 and 60 irreducible **k** points, respectively, representing only 1% of the IBZ. An extreme scenario is represented by band dispersions with small effective masses for which very high resolution in **k** space is needed to sample the small electron (hole) pockets. For instance, in GaAs, due to the very small electron effective mass ($\sim$0.053 m_0 with m_0 the free electron mass), the effective number of **k** points reduces to around 0.05% of the IBZ. This class of systems is challenging also for Wannier-based approaches as is apparent from the large discrepancy in the results for the electron mobility in GaAs reported by different authors [22,28,66]. In our implementation, we can treat systems with small effective masses with the following procedure. We start with a NSCF calculation on a reasonably dense **k** mesh to determine the position of the band edges within a certain tolerance. Then we use the SKW method [59–61] to interpolate electron energies on a much denser **k** grid. This step allows us to identify the **k** points lying inside a predefined energy window around the band edges. Finally, a second NSCF calculation for this restricted set of wave vectors is performed and the resulting (exact) KS wave functions and energies are used to compute lifetimes and transport properties.[6] We note that all the calculations reported in this work have been performed without this procedure because mobility computations in Si and GaP do not need particularly dense **k** grids to converge. We were also able to reach converged computations in the worst-case scenario of GaAs without employing this technique despite the increased computational cost of the NSCF calculation. It is however evident that e-ph calculations in more challenging systems characterized by small effective masses and/or larger unit cells will benefit from this SKW-based approach.

The reduction in the number of **k** points already leads to a large speed-up but another, distinct, optimization can be implemented when computing the imaginary part of the SE. For a fixed **k** point, indeed, not all **q** points are compatible with energy conservation [65]. This selection rule is schematically depicted in Fig. 1(b). Thanks to the tetrahedron method, it is possible to identify, for a given **k** point, the subset of **q** points in the IBZ$_\mathbf{k}$ contributing to Eq. (26).[7] This filtering technique restricts the computation of the matrix elements $g_{mn\nu}(\mathbf{k}, \mathbf{q})$ to

---

[6] The set of **k** points obtained with this procedure belongs to a homogeneous mesh hence both symmetries and tetrahedron method can be used without any modification. Small errors in the tetrahedron weights may be introduced by the linear interpolation because **k** points that are slightly outside of the energy window are interpolated with SKW but this minor issue can be easily fixed by enlarging the energy window. This techniques permits to reach very high resolution in **k** space of the order of $300 \times 300 \times 300$.

[7] In principle, a similar optimization can be implemented for the Lorentzian and Gaussian broadening techniques, however this requires choosing a threshold beyond which the broadened δ is treated as zero.
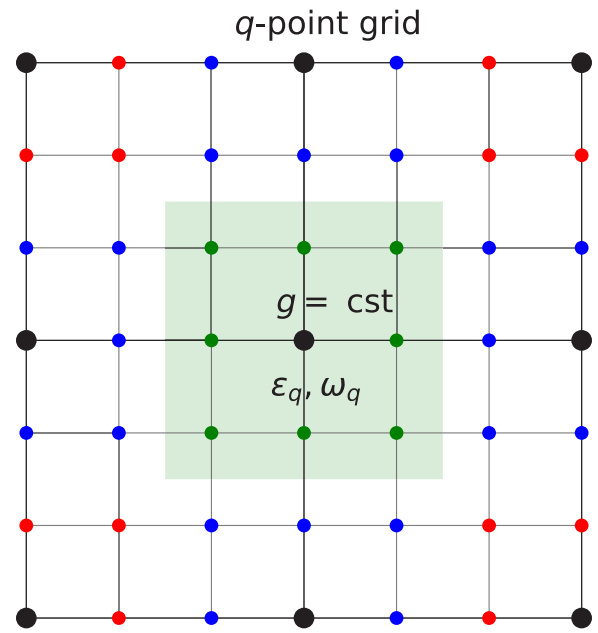

FIG. 2. Schematic representation of the DG technique. Black dots represent **q** points belonging to the coarse grid where the e-ph matrix elements $g_{mn\nu}(\mathbf{k}, \mathbf{q})$ are explicitly computed using our interpolation procedure. Colored small dots are **q** points of the fine grid where the $g_{mn\nu}(\mathbf{k}, \mathbf{q})$ are assumed to be constant in the region surrounding the black dot (the shaded green area).

a small set of **q** points in the IBZ$_\mathbf{k}$. The achievable reduction depends on the band structure and phonon dispersion, but in most cases only a few percents of the total number of **q** points pass this filter. In Si, for instance, less than 2% of the IBZ$_\mathbf{k}$ needs to be taken into account when evaluating the imaginary part of the SE thus leading to an additional significant speedup. In GaAs, the reduction is even larger thanks to the highly dispersive band centered at Γ that allows for only a few intravalley transitions. In this case, less than 0.2% of the IBZ$_\mathbf{k}$ has to be considered for each **k** point.

D. Double-grid technique

The evaluation of $\varepsilon_{n\mathbf{k}}$ and $\omega_{\mathbf{q}\nu}$ is computationally less demanding than that of $g_{mn\nu}(\mathbf{k}, \mathbf{q})$. This is evident in our implementation where the evaluation of Eq. (5) requires the electron wave functions and the derivative of the potential to be stored in memory to apply the first-order KS Hamiltonian. To improve the convergence rate without increasing the computational cost, we implemented the possibility to use different **q** meshes: one coarse mesh for $g_{mn\nu}(\mathbf{k}, \mathbf{q})$ and a finer one to describe the absorption and emission terms in Eq. (26) where only $\varepsilon_{m\mathbf{k}+\mathbf{q}}$ and $\omega_{\mathbf{q}\nu}$ are needed. This method, already implemented in the context of Bethe-Salpeter calculations [55,67,68] and used by Fiorentini et al. [69] in the context of e-ph computations, is commonly referred to as a double-grid (DG) technique and is explained schematically in Fig. 2. The rationale behind such a technique is that, apart from the Fröhlich divergence, the e-ph matrix elements are expected to vary smoothly when compared to the Dirac δ functions in Eq. (26). Obviously this approximation breaks

down in the region around $\mathbf{q} = \Gamma$ in polar semiconductors, where a high-resolution sampling would be required to capture the divergence. Theoretically, it would be possible to address this issue by analytically integrating the diverging matrix elements close to Γ, or to compute the LR part of the matrix elements (as defined in Ref. [52]) on the fine mesh used for the DG technique. These extensions of the DG method are left for future studies. For reasons of computational performance and reliability of the results, we only allow commensurate grids. The phonon frequencies are obtained on the fine grid by interpolating the dynamical matrix in $\mathbf{q}$ space at negligible cost. The electron energies $\varepsilon_{m\mathbf{k}+\mathbf{q}}$ on the fine grid can be obtained either from a NSCF calculation or interpolated using the SKW method [59–61]. This technique offers enough efficiency and flexibility to perform fast approximate computations of the electron lifetimes for screening purposes with the additional benefit that the accuracy can be systematically improved by densifying the coarse grid for $g_{mn\nu}(\mathbf{k}, \mathbf{q})$. The following convention is used throughout this work: the $\mathbf{q}$ mesh used for the DFPT computations is called the initial mesh, while the meshes onto which the Fourier interpolation and the NSCF computations are performed are called the dense meshes. When referring to results obtained with the DG technique, the mesh used for the KS wave functions and the e-ph matrix elements is called the coarse mesh while the mesh used for the $\varepsilon_{m\mathbf{k}+\mathbf{q}}$ energies and the $\omega_{\mathbf{q}\nu}$ frequencies is denoted as the fine mesh.

E. Parallelization

Our implementation uses five different MPI levels to distribute both the workload and the most memory-demanding data structures. By default, the code distributes the $\mathbf{q}$ points in the dense IBZ to reduce the memory allocated for the scattering potentials and the computational cost for the integrals in $\mathbf{q}$ space. This parallelization level is quite efficient but tends to saturate when the number of MPI processes becomes comparable to the typical number of $\mathbf{q}$ points used to integrate the self-energy. In this regime, indeed, the wall-time required to compute the matrix elements becomes negligible and nonscalable parts such as the computation of the tetrahedron weights and symmetry tables begin to dominate. In this case, one can activate the parallelization over $\mathbf{k}$ points and spins to achieve better parallel efficiency. Calculations of the SE at different $\mathbf{k}$ points and spins are completely independent hence these two MPI levels are embarrassingly parallel with excellent scalability, albeit they do not lead to any additional decrease in the memory requirements. If memory is of concern, one can employ the MPI distribution over perturbations to parallelize the computation of the e-ph matrix elements over the (κ, α) index and distribute the corresponding scattering potentials. Finally, an additional distribution scheme over the band index m is available when the real part of the SE is computed by summing over empty states.

V. RESULTS

A. Computational details

For all computations, we used norm-conserving pseudopotentials of the Troullier-Martins type [70] in the
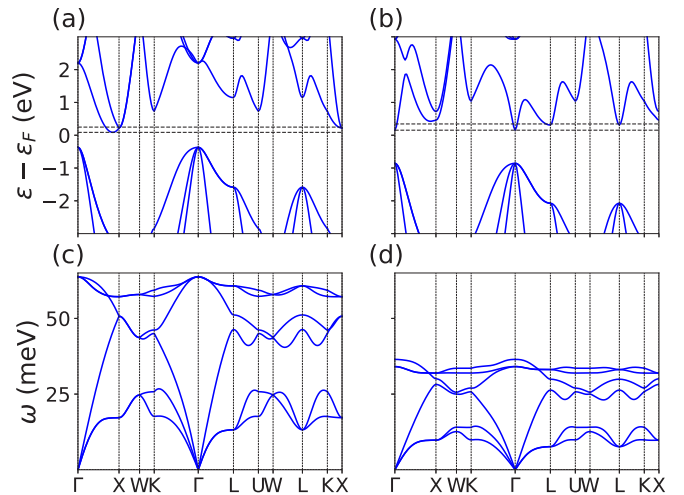

FIG. 3. Band structure of (a) Si and (b) GaAs. The Fermi level is located so that $n_e = 10^{18}$ and 10^{15} cm^{-3} for Si and GaAs, respectively. The energy window used to filter the $\mathbf{k}$ points for transport computations is represented by horizontal dashed lines. Phonon dispersions of (c) Si and (d) GaAs.

local-density approximation (LDA) from Perdew and Wang [71] parametrized by Ceperley and Alder [72], with a plane-wave kinetic energy cutoff of 20 Ha for Si and 30 Ha for GaP and GaAs. The use of LDA pseudopotentials without nonlinear core corrections is imposed by the current implementation of the dynamical quadrupoles. The theoretical values of $Q_{\kappa\alpha}^{\beta\gamma}$ used in this work are given in Ref. [73]. The relaxed lattice parameter is 5.38 Å for Si, 5.32 Å for GaP, and 5.53 Å for GaAs. To obtain an accurate Fourier interpolation of the e-ph scattering potentials, we use $9 \times 9 \times 9$ DFPT $\mathbf{q}$ grids for Si and GaP and $6 \times 6 \times 6$ for GaAs. The choice of the initial DFPT grid is based on the study reported in Ref. [41]. In the next sections, we discuss our results for Si and GaAs, the detailed results for GaP can be found in Ref. [73]. The ABINIT band structures of Si and GaAs, are represented in Figs. 3(a) and 3(b), respectively, while the phonon dispersions are shown in panels (c) and (d). The ABIPY python library [74] has been used to automate part of the calculations as well as the post-processing of the results.

B. Carrier linewidths

In Fig. 4, we report the linewidths for states within 90 meV from the conduction band minimum (CBM) of Si obtained with different integration schemes. Close to the CBM, for energies $\varepsilon - \varepsilon_{\text{CBM}} < \omega_{\text{LO}}$ (the frequency of the longitudinal optical phonon), the linewidths are small as few scattering channels are available. For higher energies, optical-phonon emission becomes possible and leads to an increase in the linewidths around $\varepsilon = \varepsilon_{\text{CBM}} + \omega_{\text{LO}}$, which corresponds to 64 meV above the CBM of Si. As expected, the values obtained with the Lorentzian function approach the tetrahedron results when the broadening is reduced provided the $\mathbf{q}$ mesh is dense enough. A similar study with Gaussian broadening is performed in Ref. [73] where similar conclusions are reached [73].
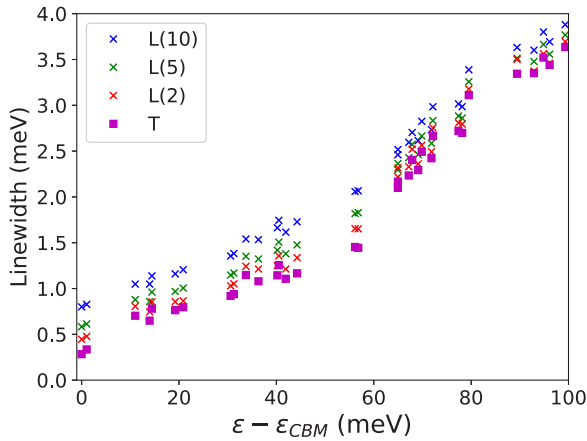
FIG. 4. Electron linewidths near the CBM of Si obtained with a $60 \times 60 \times 60$ **k**-point grid at $T = 300$ K. A very dense $180 \times 180 \times 180$ **q**-point grid is used for all curves to achieve well-converged results. Results are obtained with Lorentzian (L) and tetrahedron (T) methods. The broadening parameter is given in parentheses in meV.

In Fig. 5, we compare the convergence rate of the tetrahedron integration scheme with the one obtained with a Lorentzian broadening of 5 meV. The plot shows the average and maximum errors on the linewidths in Si and GaAs as a function of the **q** mesh used to evaluate Eq. (26). The **k** mesh for which the linewidths are obtained is fixed, and the dense **q** mesh used for integrating Eq. (25) is progressively increased until convergence is reached. In order to do this, we perform a NSCF computation for each dense mesh in order to have access to $\varepsilon_{m\mathbf{k}+\mathbf{q}}$ and $g_{mn\nu}(\mathbf{k}, \mathbf{q})$ on the dense mesh, and select the $n\mathbf{k}$ states belonging to the $9 \times 9 \times 9$ mesh to compute the linewidths. Two conclusions can be drawn from these results. (i) In both materials, the tetrahedron method outperforms the Lorentzian broadening since convergence is reached with less dense **q**-point grids. (ii) The convergence in GaAs is slower than in Si because of the integrable Fröhlich singularity for $\mathbf{q} \to \mathbf{0}$ present in polar semiconductors. This is somehow expected as the numerical integration of the singularity requires dense **q** meshes to sample enough points in the region around Γ.

At this point, it is worth comparing the convergence rate of the standard tetrahedron scheme with that obtained with the DG technique presented in Sec. IV D. Figure 6 gives the error on the linewidths in Si and GaAs, similarly to Fig. 5, but now obtained with the tetrahedron method together with the DG technique.[8] We observe that, in Si, using a $18 \times 18 \times 18$ coarse **q** grid for the e-ph matrix elements and a fine $36 \times 36 \times 36$ **q** grid for the KS energies and phonon frequencies reduces the average error below 1 meV with a computational cost very similar to that required by $18 \times 18 \times 18$ **k**- and **q**-point meshes. Increasing the density of the coarse grid further reduces the error down to practically zero. In the case of GaAs, a denser coarse **q**-point grid is required to reduce

---

[8]In all the calculations using the DG method, the KS eigenvalues on the fine **k** mesh have been computed exactly by performing a NSCF computation.
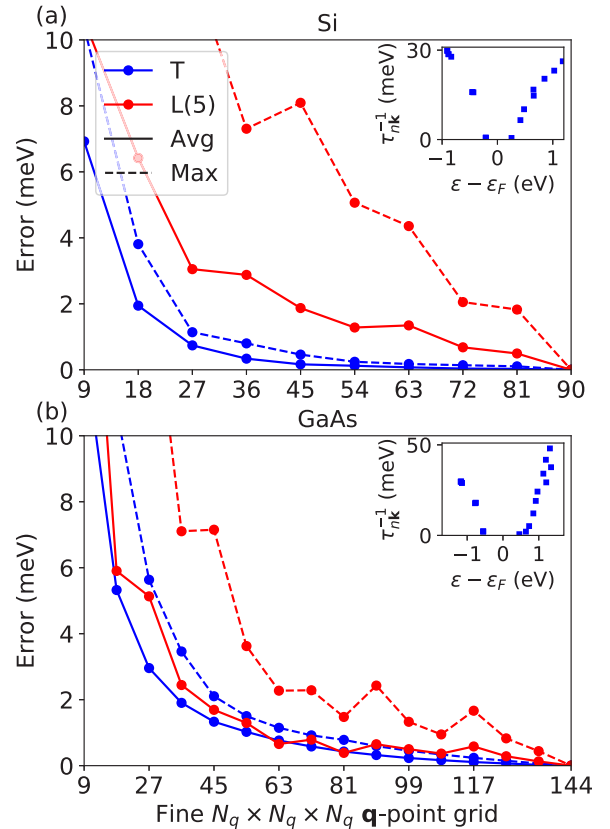

FIG. 5. Average (solid line) and maximum (dashed line) error on the linewidths evaluated on a $9 \times 9 \times 9$ **k**-point grid in (a) Si and (b) GaAs as a function of the **q** grid used for the integration. Only states within 1 eV from the CBM and VBM are considered. Results have been obtained with the tetrahedron method (T, blue) and a Lorentzian (L, red) broadening of 5 meV. The reference linewidths for each curve are the results obtained with the densest **q** grid and the corresponding integration technique. The insets show the linewidths obtained with the tetrahedron method and the densest **q** grid.

the error because of the singularity around Γ. The density of **k** points used in these tests is not large enough to converge transport properties (as shown in the next section) but it is clear that a sufficiently fine **q** mesh is important to achieve accurate linewidths whose quality will affect the final results for the mobility.

C. Phonon-limited mobility

For the computation of lifetimes and mobility, we consider an electron concentration of 10^{18} cm^{-3} both in Si and GaP, following the approach used for effective mass computations in previous works [75–77]. This choice, indeed, helps avoiding numerical noise and allows one to reach faster convergence when compared to calculations done with lower concentrations. Note, however, that the computed mobility does not correspond to the experimental one measured for 10^{18} electrons per cm^3, because such concentrations require impurities in the crystal that would increase the scattering rates and decrease the mobility. The results are representative of the intrinsic mobility as long as the Fermi level remains inside the band gap and far enough from the band edges (see
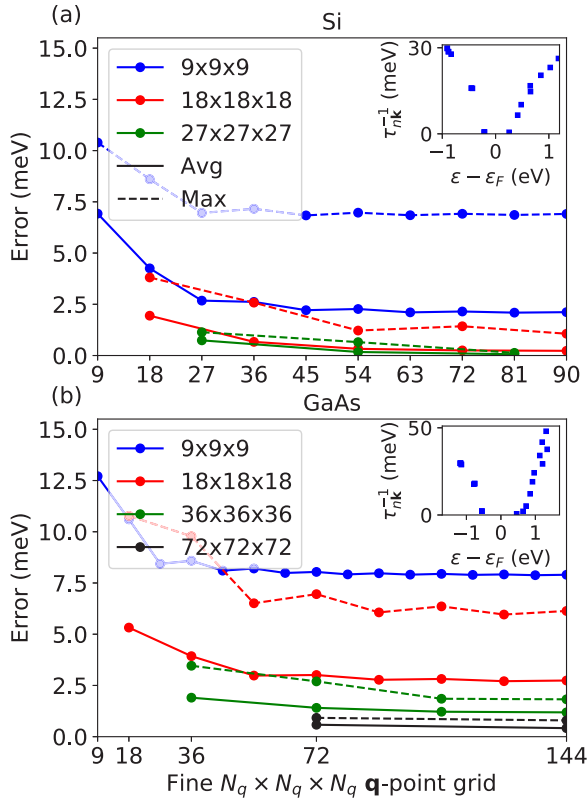
FIG. 6. Average (solid line) and maximum (dashed line) error on the linewidths on a $9 \times 9 \times 9$ **k**-point grid in (a) Si and (b) GaAs as a function of the fine **q**-point grid used for the integration. The matrix elements are obtained on (a) coarse $9 \times 9 \times 9$ (blue), $18 \times 18 \times 18$ (red) and $27 \times 27 \times 27$ (green) grids for Si and (b) coarse $9 \times 9 \times 9$ (blue), $18 \times 18 \times 18$ (red) $36 \times 36 \times 36$ (green) and $72 \times 72 \times 72$ (black) grids for GaAs. KS energies are computed on the fine grids. Only states within 1 eV from the CBM and VBM are considered. The reference linewidths (insets) are the results obtained with a $90 \times 90 \times 90$ ($144 \times 144 \times 144$) **q**-point grid for both matrix elements and energies for Si (GaAs).

FIG. 7. (a) xx component of the integrand in Eq. (28) convoluted with $\delta(\varepsilon - \varepsilon_{n\mathbf{k}})$ in the conduction band of Si, for $24 \times 24 \times 24$ (black), $48 \times 48 \times 48$ (red), and $72 \times 72 \times 72$ (green) **k**-point and $144 \times 144 \times 144$ **q**-point grids at $T = 300$K. (b) Electron mobility of Si as a function of the energy window used for the computation of the lifetimes in Eq. (28). $72 \times 72 \times 72$ **k**-point and $144 \times 144 \times 144$ **q**-point grids have been used. For these grids, the converged value is 1509 cm^2 V^{-1} s^{-1}. A 160-meV energy range is enough to reach a relative error in the mobility lower than 1%.

also the tests reported in Ref. [73]). In GaAs, we used an electron concentration of 10^{15} cm^{-3} because the density of states in the conduction band is very small.

In our implementation, as mentioned in Sec. IV C, lifetimes and group velocities are computed only for the KS states that contribute to Eq. (28) by introducing an energy window around the Fermi level. Figure 7(a) shows the convergence of the integrand of Eq. (28) (convoluted by $\delta(\varepsilon - \varepsilon_{n\mathbf{k}})$ as discussed in Appendix D) for increasing **k**-point densities, in the case of electrons in the conduction band of Si. Integrating this function directly gives the electron mobility. Figure 7(a) shows that the integrand quickly vanishes for energies far from the Fermi level (and, therefore, far from the CBM). As a consequence, it is possible to find an optimal energy window for the electrons that leads to a considerable computational saving without affecting the quality of the calculation. This is demonstrated in Fig. 7(b) where we report the mobility obtained for different values of the window. In Si, an energy range of 0.16 eV is sufficient to reach less than 1% relative error on the mobility while a slightly larger value of 0.19 (0.18) eV is needed for GaAs (GaP). We therefore use these
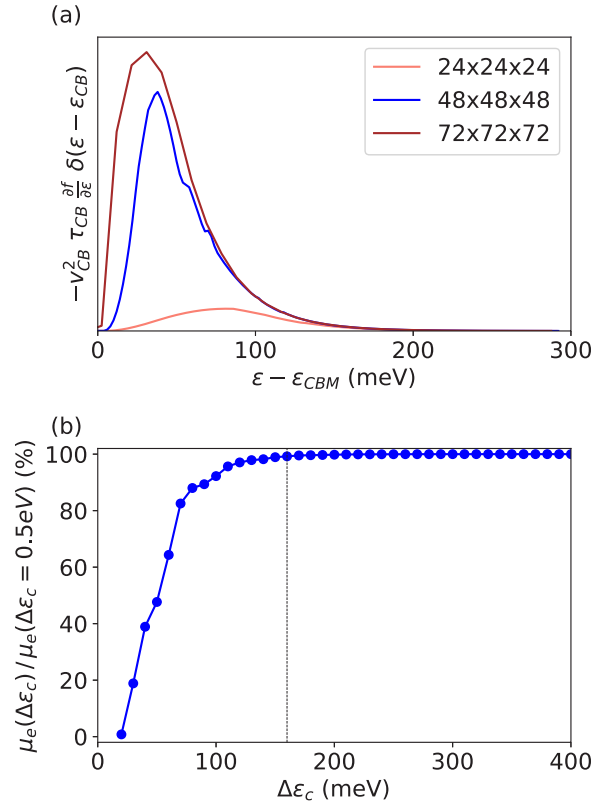
values for the energy window and, hereafter, we focus on the convergence of the electron mobility with respect to the **k** and **q** meshes, including a detailed analysis of the effect of the DG integration scheme on the convergence rate.

Figure 8 shows the dependence of the electron mobility in Si on the equivalent **k** grid used for the integration of Eq. (28), as well as on the dense **q** mesh used for the evaluation of the lifetimes [Eq. (27)]. The mesh of **q** points is the same as the **k** grid (black dots), or twice as dense in each direction (red crosses). For a given **k** grid, increasing the **q**-point density (compare vertically aligned data points in Fig. 8) systematically decreases the mobility as more scattering channels are included. We need to include a sufficient number of **k** wave vectors to evaluate Eq. (28) and enough **q** points to evaluate Eq. (27). All the convergence curves shown in Fig. 8 follow the same trend: at low **k**-point densities, the (unconverged) mobility increases with the **k**-point density. This is because the **k**-point sampling of the conduction band becomes denser close to the CBM where the integrand of Eq. (28) reaches its maximum [see Fig. 7(a)]. Once the number of **k** points included in the computation of the mobility is large enough, the mobility starts to decrease because the density of **q**

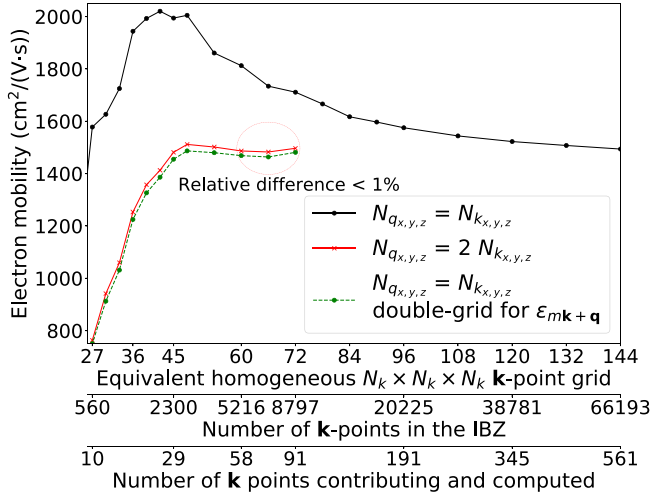FIG. 8. Electron mobility in Si ($T = 300$ K) as a function of the **k**- and **q**-point grids. The density of **q** points is the same as the density of **k** points (black), or twice as dense (red). The results obtained with DG technique are also reported (green, dashed). In this case, the densities of the **k**- and **q**-point grids are the same for matrix elements and lifetimes, but a grid twice as dense is used for the energies in Eq. (26). The equivalent homogeneous **k** mesh is first reported, together with the corresponding number of points in the IBZ. The effective number of **k** points included in the computation of $\tau_{n\mathbf{k}}$ is also given.

FIG. 9. Electron mobility in GaAs ($T = 300$ K) as a function of the **k**- and **q**-point grids. The density of **q** points is the same as the density of **k** points (black), twice (red), or three times (blue) as dense in each direction. The DG technique results are also reported (green, dashed). In this case, the densities of the **k**- and **q**-point grids are the same for e-ph matrix elements and lifetimes, but a grid twice as dense in all directions is used for the energies in Eq. (26). The equivalent homogeneous **k** mesh is reported, together with the corresponding number of points in the IBZ. The effective number of **k** points included in the computation of $\tau_{n\mathbf{k}}$ is also given.

points increases and more scattering channels are properly captured.

The total number of **k** points in the IBZ is reported on the second *x* axis of Fig. 8, together with the effective number of **k** points included in the integration of Eq. (28) (third *x* axis). Note that only around 1% of the IBZ needs to be computed. The red curve (obtained with a **q** mesh twice as dense in each direction as the **k** mesh) shows that convergence within 1% is achieved with a $60 \times 60 \times 60$ **k** mesh together with a $120 \times 120 \times 120$ **q** grid. Using a $45 \times 45 \times 45$ grid for electrons and a $90 \times 90 \times 90$ grid for phonons already leads to an error lower than 5%. We conclude that, in Si, a **q** mesh twice as dense in each direction as the **k** mesh is required to accelerate convergence. If the mobility is computed with the same mesh for electrons and phonons, indeed, the convergence is much slower as we include an unnecessarily large number of **k** points whose lifetimes are still far from convergence.

The mobility obtained with the DG technique for the lifetimes is also reported (dashed green line). In this case, the density of **k** and **q** points is the same for the lifetimes and the e-ph matrix elements, but now the **q**-point density is doubled in each direction for the energies in Eq. (26), thus allowing a better description of phonon absorption and emission processes. The results are almost identical to those obtained by explicitly computing the e-ph matrix elements on the same grid as the energies (red). To appreciate the efficiency of the DG integration scheme, it is worthwhile to compare the wall-time required by two calculations done with the same sampling. The computation time of a standard e-ph calculation in Si with a $45 \times 45 \times 45$ **k** grid and a $90 \times 90 \times 90$ **q** mesh using a single CPU is around 2 hours

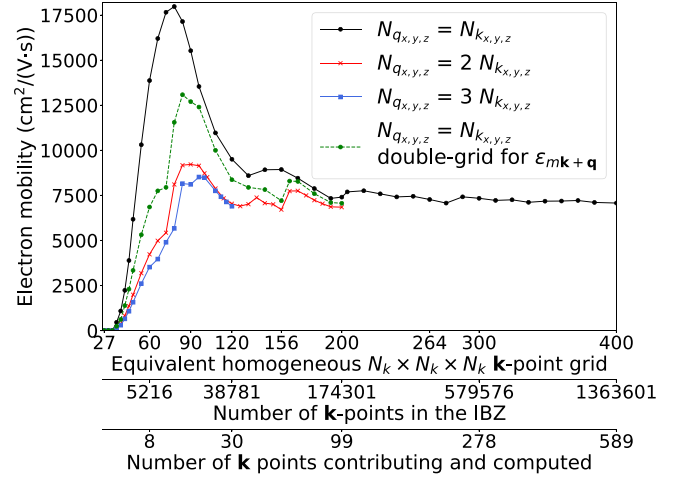and decreases down to 40 minutes when the DG technique is used. Obviously, the wall-time can be easily decreased by running on multiple CPUs using the MPI implementation discussed in Sec. IV E.

Our converged value for the electron mobility in Si is 1509 cm^2 V^{-1} s^{-1} that compares well with experimental data comprised between 1300 and 1450 cm^2 V^{-1} s^{-1} [26]. Our results are consistent with other theoretical SERTA calculations reported in the literature that range from 1555 and 1872 cm^2 V^{-1} s^{-1} [22,23,26]. For the sake of completeness, one should also stress that mobilities are quite sensitive to the computational parameters. Poncé *et al.* showed that, in Si, the choice of the XC functional can lead to a difference of about 10% in the mobility [26]. The lattice parameter also has a large effect as well as the formalism used to compute the electronic dispersion (for example, LDA versus *GW*).

We now discuss our results for the electron mobility in GaAs that are summarized in Fig. 9. First of all, we note that, despite the very dense homogeneous **k** mesh employed, a relatively small number of effective **k** points contribute and therefore need to be computed. As explained in Sec. IV C, this is due to the small effective mass (high dispersion) of the CB in GaAs. The blue curve in Fig. 9 has been obtained with a **q** mesh that is three times denser than the **k** mesh in each direction. For the $108 \times 108 \times 108$ **k** grid, the red and blue curves give very similar results thus confirming that a $216 \times 216 \times 216$ **q** mesh is dense enough for an accurate integration of the linewidths. Note, however, that a $216 \times 216 \times 216$ **k** mesh for electrons is not sufficient to converge the mobility. Convergence within 5% is indeed reached with a $264 \times 264 \times 264$ **k** mesh (and the same **q** mesh). The mobility obtained using the DG technique is also reported in
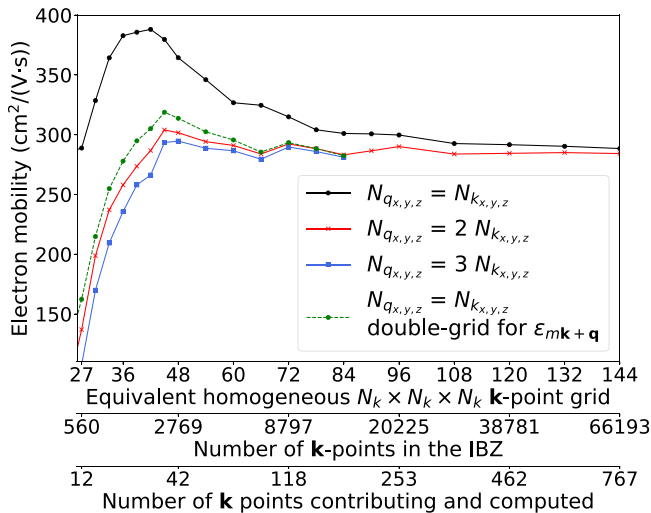
FIG. 10. Electron mobility in GaP ($T = 300$ K) as a function of the **k**- and **q**-point grids. The density of **q** points is the same as the density of **k** points (black), twice (red), or three times (blue) as dense in each direction. The DG technique results are also reported (green, dashed). In this case, the densities of the **k**- and **q**-point grids are the same for matrix elements and lifetimes, but a grid twice as dense in all directions is used for the energies in Eq. (26). The equivalent homogeneous **k** mesh is reported, together with the corresponding number of points in the IBZ. The effective number of **k** points included in the computation of $\tau_{n\mathbf{k}}$ is also given.

Fig. 9 (green dashed line). The results with the double grid are systematically improved (closer to red crosses, compared to black dots). Unfortunately, the convergence of the double grid is not as smooth and fast as the one observed in Si, likely due to the divergence of the e-ph matrix elements around Γ. Our final value for the electron mobility in GaAs obtained with a $400 \times 400 \times 400$ grid both for electrons and phonons is 7075 cm^2 V^{-1} s^{-1}. This result is in the range of reported electron mobilities for GaAs, roughly between 7000 and 12 000 cm^2 V^{-1} s^{-1} [22,38,66]. The large range of computed mobilities has been analyzed in Ref. [22]. The lattice parameter has a very important role, as well as the formalism used both for the electronic band structure (GGA, GW, etc.) and the transport computation (iterative BTE, momentum-relaxation time approximation, etc.). In addition, we use the tetrahedron integration method and treat dynamical quadrupoles in the interpolation of the scattering potentials.

Finally, in Fig. 10, we report the electron mobility in GaP. This system is less problematic than GaAs and convergence within 5% is reached with $54 \times 54 \times 54$ **k**-point and $108 \times 108 \times 108$ **q**-point meshes. Oscillations are still observed for **k** meshes denser than $78 \times 78 \times 78$, but not larger than 2%. For these grids, the **q**-point mesh is well converged, as shown by the blue curve (**q** mesh three times as dense in each direction as the **k** mesh). The mobility obtained with the DG technique is also reported in the same figure (green dashed line). Once the **q** mesh is dense enough to correctly describe this divergence ($66 \times 66 \times 66$ mesh), the DG results are very similar to a full computation taking into account the variation of the e-ph matrix elements on a **q** mesh twice as dense as the **k** mesh (red crosses). There are few experimental data

for the electron mobility in GaP with values between 200 and 330 cm^2 V^{-1} s^{-1} [78] but experiments are usually performed on polycrystalline samples. A more accurate description of transport properties in GaP would therefore require the inclusion of grain-boundary scattering effects that are beyond the scope of the present work. It is clear that additional theoretical work and more advanced *ab initio* techniques including self-consistency in the Boltzmann transport equation, many-body effects in the electron-electron interaction as well as additional scattering processes are needed in order to improve the agreement between theory and experiment. Nonetheless, our convergence studies for the phonon-limited electron mobility in Si and GaP indicate that the **q** mesh should be at least as dense as the **k** mesh in order to capture enough scattering channels with small momentum transfer. In GaAs, a very fine **k** mesh is required due to the high dispersion of the conduction band. In this case, it is not as interesting to use a denser **q** mesh.

VI. CONCLUSION

We present an efficient method based on plane waves and Bloch states for the computation of the e-ph self-energy and carrier mobilities in the self-energy relaxation time approximation. Our approach takes advantage of symmetries and advanced integration techniques such as the linear tetrahedron and double-grid methods to achieve accurate results with a computational cost that is competitive with state-of-the-art implementations based on localized orbitals. The number of explicit DFPT calculations is significantly reduced by interpolating the scattering potentials using a real-space representation in conjunction with Fourier transforms while Bloch states are treated exactly. A systematic analysis of the convergence behavior of electron linewidths and mobilities in Si, GaAs and GaP as a function of the initial *ab initio* **q** mesh reveals that the proper treatment of the long-range fields due to dynamical quadrupoles is crucial for an accurate and efficient interpolation in the region around Γ [41]. We discussed how to treat quadrupolar terms in e-ph calculations in a fully *ab initio* way using the recently proposed first-principles theory of spatial dispersion [53]. Our approach is implemented as direct post-processing of standard DFPT calculations and the e-ph results can be easily converged by monitoring a small set of parameters defining the BZ sampling and an energy window around the Fermi level. Smart sampling techniques and highly parallel algorithms make it possible to obtain converged carrier mobilities for relatively small crystalline systems in a few hours with commodity-class clusters. Our work will hopefully pave the way towards systematic and high-throughput studies of materials properties related to e-ph interaction both in polar and nonpolar semiconductors.

Note added. Recently, we became aware of a related work by another group that reaches similar conclusions about the importance of the dynamical quadrupole term to obtain an accurate physical description of e-ph interactions [89,90].

ACKNOWLEDGMENTS

APPENDIX A: LONG-WAVELENGTH LIMIT IN SEMICONDUCTORS

1. DFPT potentials for $q \to 0$

In the e-ph scattering potentials, there are two different nonanalytic terms in $\mathbf{q}$ space. The derivative of the local part of the pseudopotential, $\partial_{\kappa\alpha,\mathbf{q}} v^{\mathrm{loc}}$, behaves like [51,53,79]:

$$\partial_{\kappa\alpha,\mathbf{q}} v^{\mathrm{loc}}(\mathbf{G} = \mathbf{0}) = i\frac{4\pi}{\Omega}\frac{q_\alpha}{q^2}Z_\kappa + \mathcal{O}(q_\alpha), \qquad (A1)$$

with Z_κ the charge of the (pseudo) ion κ. The second term is the derivative of the Hartree potential $\partial_{\kappa\alpha,\mathbf{q}} v^{\mathrm{H}}$ that is linked to the density variation by a simple formula in reciprocal space:

$$\partial_{\kappa\alpha,\mathbf{q}} v^{\mathrm{H}}(\mathbf{G}) = \frac{4\pi}{|\mathbf{q}+\mathbf{G}|^2}\partial_{\kappa\alpha,\mathbf{q}} n(\mathbf{G}). \qquad (A2)$$

The $\mathbf{G} = \mathbf{0}$ component of the density change is therefore amplified by a diverging $4\pi/q^2$ factor. This is handled in DFPT by the separate treatment of the screened electric field as discussed in Refs. [15,51,79]. This term is subtracted in auxiliary DFPT computations, as explained in Sec. II C. In principle, there is also a $1/q^2$ contribution coming from the (exact) XC kernel but approximated functionals such as LDA or GGA fail to reproduce such behavior [79,80]. The nonlocal part of the pseudopotential is short-ranged in real space and does not pose additional challenges.

2. Derivations of Eqs. (15) and (16)

Equation (15) can be obtained by the combination of different equations coming from Appendix A of Ref. [15]. Namely, one should use Eqs. (A5), (A6), (A26), (A51), (A54), (A73), and (A66), rewritten here with the notation of this paper. The first-order derivatives of the wave functions with respect to collective oscillations for $\mathbf{q} \to 0$ are obtained as

$$\left|u_{n\mathbf{k},\mathbf{q}\to\mathbf{0}}^{\tau_{\kappa\alpha}}\right\rangle = -\mathbf{A}^{-1}\mathbf{w} + \frac{-b+a(\mathbf{u}^\dagger\mathbf{A}^{-1}\mathbf{w})}{1+a(\mathbf{u}^\dagger\mathbf{A}^{-1}\mathbf{u})}\mathbf{A}^{-1}\mathbf{u}, \qquad (A3)$$

where the definitions of $\mathbf{A}$, $\mathbf{w}$, $\mathbf{u}$, a and b can be found in Ref. [15]. The denominator in the previous equation is the $\mathbf{q}$-dependent macroscopic dielectric function:

$$\epsilon_M(\mathbf{q}) = 1 + a(\mathbf{u}^\dagger\mathbf{A}^{-1}\mathbf{u}). \qquad (A4)$$

The numerator is given by extending Eq. (A73) of Ref. [15] to the next order in q:

$$-b + a(\mathbf{u}^\dagger\mathbf{A}^{-1}\mathbf{w}) = -\frac{4\pi iq_\gamma}{\Omega q^2}Z_{\kappa\alpha,\gamma}^* e^{-iq_\eta\tau_{\kappa\eta}}. \qquad (A5)$$

The first term in Eq. (A3) is the first-order wave function due to collective atomic displacements at $\mathbf{q} = \mathbf{0}$, where the $\mathbf{G} = \mathbf{0}$ term of the Hartree potential change has been removed:

$$-\mathbf{A}^{-1}\mathbf{w} = \left|u_{n\mathbf{k},\mathbf{q}=\mathbf{0}}^{\tau_{\kappa\alpha}'}\right\rangle, \qquad (A6)$$

and $\mathbf{A}^{-1}\mathbf{u}$ is the same first-order wave function but with an electric field perturbation:

$$\mathbf{A}^{-1}\mathbf{u} = -i\mathcal{Q}q_\lambda\left|u_{n\mathbf{k}}^{\mathcal{E}_\lambda'}\right\rangle. \qquad (A7)$$

Inserting Eqs. (A4)–(A7) into Eq. (A3) gives Eq. (15) of the main text. Note that the electric field perturbation in Eqs. (15) and (A7) has been defined following the convention of Ref. [53], that differs from the convention of Ref. [79]. The difference is the charge of the electron, that has already been included in the latter. In Ref. [79], the perturbation might be better referred to as the $\mathcal{Q}\mathcal{E}_\alpha$ perturbation. So, in this sense, ABINIT implements the $\mathcal{Q}\mathcal{E}_\alpha$ perturbation and not the $\mathcal{E}_\alpha$ perturbation.

Equation (16) is obtained using Eq. (A4) and extending

$$-b + a(\mathbf{u}^\dagger\mathbf{A}^{-1}\mathbf{w}) \qquad (A8)$$

in Eq. (A5) to the cell-integrated charge response to a monochromatic atomic displacement from Eq. (17).

APPENDIX B: SYMMETRY PROPERTIES OF THE WAVE FUNCTIONS

In this Appendix, we discuss how to use symmetries to reconstruct KS eigenvalues and wave functions in the full BZ from the IBZ. We focus on scalar wave functions, the generalization to two-component spinors is discussed in Ref. [81].

A generic element of the crystalline space group will be denoted in the following with the $\hat{\mathcal{S}}_{\mathbf{f}}$ symbol where $\mathcal{S}$ is a real orthonormal matrix corresponding to a proper or improper rotation and $\mathbf{f}$ the associated fractional translation in Cartesian coordinates. The application of the symmetry operator $\hat{\mathcal{S}}_{\mathbf{f}}$ to the atomic position $\boldsymbol{\tau}$ is defined by

$$\hat{\mathcal{S}}_{\mathbf{f}}\,\boldsymbol{\tau} \equiv \mathcal{S}\boldsymbol{\tau} + \mathbf{f}. \qquad (B1)$$

The inverse of $\hat{\mathcal{S}}_{\mathbf{f}}$ has rotational part $\mathcal{S}^{-1}$ and fractional translation $-\mathcal{S}^{-1}\mathbf{f}$. The application of the symmetry operation $\hat{\mathcal{S}}_{\mathbf{f}}$ on a generic function $F(\mathbf{r})$ of the three spatial coordinates $\mathbf{r}$ is conventionally defined by:

$$\hat{\mathcal{S}}_{\mathbf{f}}F(\mathbf{r}) \equiv F(\mathcal{S}^{-1}(\mathbf{r} - \mathbf{f})). \qquad (B2)$$

Since $\hat{\mathcal{S}}_{\mathbf{f}}$ commutes with the KS Hamiltonian $\hat{H}$ of the crystal, it readily follows that, given $\psi_{n\mathbf{k}}(\mathbf{r})$ eigenstate of $\hat{H}$ with eigenvalue $\varepsilon_{n\mathbf{k}}$ also $\hat{\mathcal{S}}_{\mathbf{f}}\psi_{n\mathbf{k}}(\mathbf{r})$ is eigenstate of the Schrödinger problem with the same eigenvalue:

$$\hat{H}\hat{\mathcal{S}}_{\mathbf{f}}\psi_{n\mathbf{k}} = \hat{\mathcal{S}}_{\mathbf{f}}\hat{H}\psi_{n\mathbf{k}} = \varepsilon_{n\mathbf{k}}\hat{\mathcal{S}}_{\mathbf{f}}\psi_{n\mathbf{k}}. \qquad (B3)$$

Although $\hat{\mathcal{S}}_{\mathbf{f}}\psi_{n\mathbf{k}}(\mathbf{r})$ has the same eigenenergy as $\psi_{n\mathbf{k}}(\mathbf{r})$, its crystalline momentum is different. The operator $\hat{\mathcal{S}}_{\mathbf{f}}$ transforms a Bloch eigenstate $e^{i\mathbf{k}\cdot\mathbf{r}}u_{n\mathbf{k}}(\mathbf{r})$ with vector $\mathbf{k}$ into a new Bloch

state of crystalline momentum $\mathcal{S}\mathbf{k}$. This important property can be seen as follows:

$$
\begin{aligned}
[\hat{S}_{\mathbf{f}}\psi_{n\mathbf{k}}](\mathbf{r}+\mathbf{R}) &= \psi_{n\mathbf{k}}(\mathcal{S}^{-1}(\mathbf{r}+\mathbf{R}-\mathbf{f})) \\
&= e^{i\mathbf{k}\cdot\mathcal{S}^{-1}(\mathbf{r}+\mathbf{R}-\mathbf{f})}u_{n\mathbf{k}}(\mathcal{S}^{-1}(\mathbf{r}-\mathbf{f})) \\
&= e^{i\mathcal{S}^{-1}\mathbf{k}\cdot\mathbf{R}}\psi_{n\mathbf{k}}(\mathcal{S}^{-1}(\mathbf{r}-\mathbf{f})) \\
&= e^{i\,\mathcal{S}\mathbf{k}\cdot\mathbf{R}}\hat{S}_{\mathbf{f}}\psi_{n\mathbf{k}}(\mathbf{r}),
\end{aligned} \tag{B4}
$$

where the invariance under lattice translation of the periodic part of the Bloch wave function $u_{n\mathbf{k}}(\mathbf{r})$ has been exploited. The set of equations below summarizes the relationships employed to reconstruct the wave functions in the BZ[9]

$$
\begin{aligned}
\varepsilon_{\mathcal{S}\mathbf{k}} = \varepsilon_{\mathbf{k}} u_{\mathcal{S}\mathbf{k}}(\mathbf{r}) &= e^{-i\mathcal{S}\mathbf{k}\cdot\mathbf{f}}u_{\mathbf{k}}(\mathcal{S}^{-1}(\mathbf{r}-\mathbf{f}))u_{\mathcal{S}\mathbf{k}}(\mathbf{G}) \\
&= e^{-i(\mathcal{S}\mathbf{k}+\mathbf{G})\cdot\mathbf{f}}u_{\mathbf{k}}(\mathcal{S}^{-1}\mathbf{G}),
\end{aligned} \tag{B5}
$$

where we used the following conventions for the Fourier series of periodic lattice quantities

$$
u(\mathbf{G}) = \frac{1}{\Omega}\int_{\Omega} u(\mathbf{r})e^{-i\mathbf{G}\cdot\mathbf{r}}\,d\mathbf{r}, \tag{B6}
$$

$$
u(\mathbf{r}) = \sum_{\mathbf{G}} u(\mathbf{G})e^{i\mathbf{G}\cdot\mathbf{r}}. \tag{B7}
$$

The time invariance of the Hamiltonian leads to the additional symmetries

$$
\varepsilon_{-\mathbf{k}} = \varepsilon_{\mathbf{k}}, \quad u_{-\mathbf{k}}(\mathbf{r}) = u_{\mathbf{k}}^{*}(\mathbf{r}), \quad u_{-\mathbf{k}}(-\mathbf{G}) = u_{\mathbf{k}}^{*}(\mathbf{G}), \tag{B8}
$$

that may be used to halve the number of $\mathbf{k}$ points even if the system is not invariant under spatial inversion. Finally, wave functions with $\mathbf{k}$-wave vector outside the first Brillouin zone are obtained with the gauge

$$
\psi_{n\mathbf{k}+\mathbf{G}}(\mathbf{r}) = \psi_{n\mathbf{k}}(\mathbf{r}). \tag{B9}
$$

It is important to stress that in Eqs. (B5), (B8), and (B9), we assumed nondegenerate eigenstates. In the presence of degeneracy, indeed, it is always possible to construct new orthonormal eigenstates of the Hamiltonian by performing a unitary transformation within the degenerate subspace. However, electron lifetimes (and physical observables, in general) do not depend on this gauge since all the degenerate states are summed over in Eq. (27) hence the presence of this gauge is irrelevant in our context.

APPENDIX C: SYMMETRY PROPERTIES OF THE SCATTERING POTENTIALS

Symmetry properties can also be used to reconstruct the e-ph scattering potentials from an appropriate set of atomic perturbations with wave vector $\mathbf{q}$ in the IBZ of the unperturbed crystal. For the local external potential, the derivation of the symmetry properties is particularly simple as the

lattice-periodic part of the first order derivative can be easily expressed in reciprocal space using [79]

$$
\partial_{\kappa\alpha,\mathbf{q}}v^{\mathrm{loc}}(\mathbf{G}) = -\frac{i}{\Omega}(\mathbf{q}+\mathbf{G})_{\alpha}e^{-i(\mathbf{q}+\mathbf{G})\cdot\boldsymbol{\tau}_{\kappa}}v_{\kappa}^{\mathrm{loc}}(|\mathbf{q}+\mathbf{G}|), \tag{C1}
$$

where $v_{\kappa}^{\mathrm{loc}}(|\mathbf{q}+\mathbf{G}|)$ is the Fourier transform of the local part of the pseudopotential associated to atom κ. Starting from this formula, one obtains that the Fourier component at the rotated $(\mathcal{S}\mathbf{q}, \mathcal{S}\mathbf{G})$ is given by a linear combination of the symmetry-related $(\kappa'\beta)$ terms with wave vector $\mathbf{q}$ in the IBZ

$$
\partial_{\kappa\alpha,\mathcal{S}\mathbf{q}}v^{\mathrm{loc}}(\mathcal{S}\mathbf{G}) = \sum_{\beta}\mathcal{S}_{\alpha\beta}\,\partial_{\kappa'\beta,\mathbf{q}}\,v^{\mathrm{loc}}(\mathbf{G})e^{-i(\mathbf{q}+\mathbf{G})\cdot(\mathbf{L}_0+\mathcal{S}^{-1}\mathbf{f})}, \tag{C2}
$$

where $\boldsymbol{\tau}_{\kappa'}$ denotes the position of the symmetric atom in the first unit cell and $\mathbf{L}_0$ is a, possibly null, real-space lattice vector. The two symmetric atoms at $\boldsymbol{\tau}_{\kappa}$ and $\boldsymbol{\tau}_{\kappa'}$ are related by the inverse of $\hat{S}_{\mathbf{f}}$:

$$
\mathcal{S}^{-1}(\boldsymbol{\tau}_{\kappa}-\mathbf{f}) = \boldsymbol{\tau}_{\kappa'}+\mathbf{L}_0. \tag{C3}
$$

We now derive the symmetry properties of the SCF part of the DFPT potential using Eq. (C2) and well-known results for the inverse dielectric matrix ϵ^{-1}. The first-order variation of the self-consistent potential is indeed related to the first-order change of the external potential by

$$
\delta V^{\mathrm{scf}}(\mathbf{r}) = \int d\mathbf{r}'\epsilon^{-1}(\mathbf{r},\mathbf{r}')\delta V^{\mathrm{ext}}(\mathbf{r}'), \tag{C4}
$$

where ϵ^{-1} is invariant under all the symmetry operations of the crystal:

$$
\epsilon^{-1}(\mathbf{r}+\mathbf{R},\mathbf{r}'+\mathbf{R}) = \epsilon^{-1}(\mathbf{r},\mathbf{r}'), \tag{C5}
$$

$$
\epsilon^{-1}(\hat{S}_{\mathbf{f}}\mathbf{r},\hat{S}_{\mathbf{f}}\mathbf{r}') = \epsilon^{-1}(\mathbf{r},\mathbf{r}'). \tag{C6}
$$

In Fourier space, Eq. (C6) leads to the following symmetry property [82]:

$$
\epsilon_{\mathcal{S}\mathbf{G}_1,\mathcal{S}\mathbf{G}_2}^{-1}(\mathcal{S}\mathbf{q}) = e^{+i\mathcal{S}(\mathbf{G}_2-\mathbf{G}_1)\cdot\mathbf{f}}\epsilon_{\mathbf{G}_1,\mathbf{G}_2}^{-1}(\mathbf{q}) \tag{C7}
$$

where the Fourier transform of a two-point function is defined by

$$
f_{\mathbf{G}_1,\mathbf{G}_2}(\mathbf{q}) = \frac{1}{V}\iint_{V} e^{-i(\mathbf{q}+\mathbf{G}_1)\cdot\mathbf{r}_1}\,f(\mathbf{r}_1,\mathbf{r}_2)e^{i(\mathbf{q}+\mathbf{G}_2)\cdot\mathbf{r}_2}\,d\mathbf{r}_1\,d\mathbf{r}_2, \tag{C8}
$$

and V is the volume of the Born-von Kármán supercell. In $\mathbf{G}$ space, the screened potential is related to the external perturbation by:

$$
\partial_{\kappa\alpha,\mathbf{q}}v^{\mathrm{scf}}(\mathbf{G}) = \sum_{\mathbf{G}'}\epsilon_{\mathbf{G},\mathbf{G}'}^{-1}(\mathbf{q})\partial_{\kappa\alpha,\mathbf{q}}v^{\mathrm{loc}}(\mathbf{G}') \tag{C9}
$$

Using Eqs. (C2) and (C7) in Eq. (C9), after some algebra to rearrange the different terms, one obtains that the Fourier components of the SCF part of the DFPT potential transform similarly to the local part of the pseudopotential [compare with Eq. (C2)]

$$
\partial_{\kappa\alpha,\mathcal{S}\mathbf{q}}v^{\mathrm{scf}}(\mathcal{S}\mathbf{G}) = \sum_{\beta}\mathcal{S}_{\alpha\beta}\,\partial_{\kappa'\beta,\mathbf{q}}\,v^{\mathrm{scf}}(\mathbf{G})e^{-i(\mathbf{q}+\mathbf{G})\cdot(\mathbf{L}_0+\mathcal{S}^{-1}\mathbf{f})}. \tag{C10}
$$

---

[9]In our implementation, we prefer to perform the symmetrization of the periodic part of the wave function in $\mathbf{G}$ space because the fractional translation can be easily taken into account by multiplying by a phase factor. The symmetrization in real space, on the other hand, requires a real-space FFT grid compatible with all the fractional translations of the space group.

When $\mathcal{S}\mathbf{q} = \mathbf{q}$, the equation provides a connection among atomic perturbations with the same wave vector $\mathbf{q}$ that can be used to reconstruct by symmetry all the $3N_{\text{atom}}$ potentials starting from an irreducible set. Finally, we note that the contribution associated to the nonlocal part of the pseudopotential can be computed explicitly for arbitrary $\mathbf{q}$ using the equations given in [79] hence no symmetrization is required for this term.

APPENDIX D: BOLTZMANN TRANSPORT EQUATION

An equivalent formulation of the linearized Boltzmann transport equation in the RTA uses the transport distribution function [56]:

$$L_{\alpha\beta}(\omega) = \sum_n \int \frac{d\mathbf{k}}{\Omega_{\text{BZ}}} \mathrm{v}_{n\mathbf{k},\alpha} \mathrm{v}_{n\mathbf{k},\beta} \tau_{n\mathbf{k}} \delta(\omega - \varepsilon_{n\mathbf{k}}) \qquad \text{(D1)}$$

that can be used to express the generalized transport coefficients as

$$\mathcal{L}_{\alpha\beta}^{(m)} = -\int L_{\alpha\beta}(\omega)(\omega - \varepsilon_F)^m \frac{\partial f(\omega)}{\partial \omega} d\omega. \qquad \text{(D2)}$$

The expression given in the main text (Eq. (28)) is obtained by replacing Eq. (D1) in Eq. (D2) and integrating the δ function in frequency space. The integrand represented in Fig. 7(a) of the main text is

$$-\mathrm{v}_{n\mathbf{k},\alpha} \mathrm{v}_{n\mathbf{k},\beta} \tau_{n\mathbf{k}} \frac{\partial f(\omega)}{\partial \omega} \delta(\omega - \varepsilon_{n\mathbf{k}}), \qquad \text{(D3)}$$

which corresponds to the integrand in Eq. (D2) for $m = 0$.

[1] F. Giustino, Rev. Mod. Phys. **89**, 015003 (2017).

[2] W. L. McMillan, Phys. Rev. **167**, 331 (1968).

[3] H. J. Choi, D. Roundy, H. Sun, M. L. Cohen, and S. G. Louie, Nature (London) **418**, 758 (2002).

[4] M. Lüders, M. A. L. Marques, N. N. Lathiotakis, A. Floris, G. Profeta, L. Fast, A. Continenza, S. Massidda, and E. K. U. Gross, Phys. Rev. B **72**, 024545 (2005).

[5] M. A. L. Marques, M. Lüders, N. N. Lathiotakis, G. Profeta, A. Floris, L. Fast, A. Continenza, E. K. U. Gross, and S. Massidda, Phys. Rev. B **72**, 024546 (2005).

[6] E. R. Margine and F. Giustino, Phys. Rev. B **90**, 014518 (2014).

[7] E. R. Margine, H. Lambert, and F. Giustino, Sci. Rep. **6**, 21414 (2016).

[8] E. Kioupakis, P. Rinke, A. Schleife, F. Bechstedt, and C. G. Van de Walle, Phys. Rev. B **81**, 241201(R) (2010).

[9] J. Noffsinger, E. Kioupakis, C. G. Van de Walle, S. G. Louie, and M. L. Cohen, Phys. Rev. Lett. **108**, 167402 (2012).

[10] H. Peelaers, E. Kioupakis, and C. G. Van de Walle, Appl. Phys. Lett. **100**, 011914 (2012).

[11] P. B. Allen and V. Heine, J. Phys. C **9**, 2305 (1976).

[12] P. B. Allen and M. Cardona, Phys. Rev. B **27**, 4760 (1983).

[13] S. Poncé, G. Antonius, Y. Gillet, P. Boulanger, J. Laflamme Janssen, A. Marini, M. Côté, and X. Gonze, Phys. Rev. B **90**, 214304 (2014).

[14] G. Antonius, S. Poncé, E. Lantagne-Hurtubise, G. Auclair, X. Gonze, and M. Côté, Phys. Rev. B **92**, 085137 (2015).

[15] S. Poncé, Y. Gillet, J. Laflamme Janssen, A. Marini, M. Verstraete, and X. Gonze, J. Chem. Phys. **143**, 102813 (2015).

[16] D. A. Broido, M. Malorny, G. Birner, N. Mingo, and D. A. Stewart, Appl. Phys. Lett. **91**, 231922 (2007).

[17] B. Liao, B. Qiu, J. Zhou, S. Huberman, K. Esfarjani, and G. Chen, Phys. Rev. Lett. **114**, 115901 (2015).

[18] T. Y. Kim, C.-H. Park, and N. Marzari, Nano Lett. **16**, 2439 (2016).

[19] B. Xu and M. J. Verstraete, Phys. Rev. Lett. **112**, 196603 (2014).

[20] M. Bernardi, D. Vigil-Fowler, J. Lischner, J. B. Neaton, and S. G. Louie, Phys. Rev. Lett. **112**, 257402 (2014).

[21] K. Krishnaswamy, B. Himmetoglu, Y. Kang, A. Janotti, and C. G. Van de Walle, Phys. Rev. B **95**, 205202 (2017).

[22] J. Ma, A. S. Nissimagoudar, and W. Li, Phys. Rev. B **97**, 045201 (2018).

[23] W. Li, Phys. Rev. B **92**, 075405 (2015).

[24] J. I. Mustafa, M. Bernardi, J. B. Neaton, and S. G. Louie, Phys. Rev. B **94**, 155105 (2016).

[25] B. Liao, J. Zhou, B. Qiu, M. S. Dresselhaus, and G. Chen, Phys. Rev. B **91**, 235419 (2015).

[26] S. Poncé, E. R. Margine, and F. Giustino, Phys. Rev. B **97**, 121201(R) (2018).

[27] X. Zeng, S. Zhao, Z. Li, and J. Yang, Phys. Rev. B **98**, 155443 (2018).

[28] J.-J. Zhou and M. Bernardi, Phys. Rev. B **94**, 201201(R) (2016).

[29] X. Gonze, P. Boulanger, and M. Côté, Ann. Phys. **523**, 168 (2011).

[30] X. Gonze, F. Jollet, F. A. Araujo, D. Adams, B. Amadon, T. Applencourt, C. Audouze, J.-M. Beuken, J. Bieder, A. Bokhanchuk et al., Comput. Phys. Commun. **205**, 106 (2016).

[31] X. Gonze, B. Amadon, G. Antonius, F. Arnardi, L. Baguet, J.-M. Beuken, J. Bieder, F. Bottin, J. Bouchet, E. Bousquet et al., Comput. Phys. Commun. **248**, 107042 (2019).

[32] A. Marini, Phys. Rev. Lett. **101**, 106405 (2008).

[33] A. Marini, C. Hogan, M. Grüning, and D. Varsano, Comput. Phys. Commun. **180**, 1392 (2009).

[34] P. Giannozzi, S. Baroni, N. Bonini, M. Calandra, R. Car, C. Cavazzoni, D. Ceresoli, G. L. Chiarotti, M. Cococcioni, I. Dabo et al., J. Phys.: Condens. Matter **21**, 395502 (2009).

[35] S. Poncé, E. R. Margine, C. Verdi, and F. Giustino, Comput. Phys. Commun. **209**, 116 (2016).

[36] N. Marzari, A. A. Mostofi, J. R. Yates, I. Souza, and D. Vanderbilt, Rev. Mod. Phys. **84**, 1419 (2012).

[37] M. J. Van Setten, M. Giantomassi, E. Bousquet, M. J. Verstraete, D. R. Hamann, X. Gonze, and G.-M. Rignanese, Comput. Phys. Commun. **226**, 39 (2018).

[38] L. A. Agapito and M. Bernardi, Phys. Rev. B **97**, 235146 (2018).

[39] X. Gonze, B. Amadon, P.-M. Anglade, J.-M. Beuken, F. Bottin, P. Boulanger, F. Bruneval, D. Caliste, R. Caracas, M. Côté et al., Comput. Phys. Commun. **180**, 2582 (2009).

[40] A. Eiguren and C. Ambrosch-Draxl, Phys. Rev. B **78**, 045124 (2008).

[41] G. Brunin, H. P. C. Miranda, M. Giantomassi, M. Royo, M. Stengel, M. J. Verstraete, X. Gonze, G.-M. Rignanese, and G. Hautier, Phys. Rev. Lett. **125**, 136601 (2020).

[42] G. D. Mahan, *Many-Particle Physics* (Springer, New York, 2014).

[43] A. Marini, S. Poncé, and X. Gonze, Phys. Rev. B **91**, 224310 (2015).

[44] X. Gonze and C. Lee, Phys. Rev. B **55**, 10355 (1997).

[45] S. Baroni, S. de Gironcoli, A. Dal Corso, and P. Giannozzi, Rev. Mod. Phys. **73**, 515 (2001).

[46] M. C. Payne, M. P. Teter, D. C. Allan, T. A. Arias, and J. D. Joannopoulos, Rev. Mod. Phys. **64**, 1045 (1992).

[47] F. Giustino, M. L. Cohen, and S. G. Louie, Phys. Rev. B **76**, 165108 (2007).

[48] L. Kleinman and D. M. Bylander, Phys. Rev. Lett. **48**, 1425 (1982).

[49] W. Kohn, Phys. Rev. Lett. **2**, 393 (1959).

[50] P. Vogl, Phys. Rev. B **13**, 694 (1976).

[51] M. Stengel, Phys. Rev. B **88**, 174106 (2013).

[52] C. Verdi and F. Giustino, Phys. Rev. Lett. **115**, 176401 (2015).

[53] M. Royo and M. Stengel, Phys. Rev. X **9**, 021050 (2019).

[54] J. Sjakste, N. Vast, M. Calandra, and F. Mauri, Phys. Rev. B **92**, 054307 (2015).

[55] D. Sangalli, A. Ferretti, H. Miranda, C. Attaccalite, I. Marri, E. Cannuccia, P. Melo, M. Marsili, F. Paleari, A. Marrazzo *et al.*, J. Phys. Condens. Matter **31**, 325902 (2019).

[56] G. K. H. Madsen, J. Carrete, and M. J. Verstraete, Comput. Phys. Commun. **231**, 140 (2018).

[57] N. W. Ashcroft and N. D. Mermin, *Solid State Physics*, 1st ed. (Saunders College, 1976).

[58] G. Pizzi, D. Volja, B. Kozinsky, M. Fornari, and N. Marzari, Comput. Phys. Commun. **185**, 422 (2014).

[59] D. G. Shankland, Int. J. Quantum Chem. **5**, 497 (1971).

[60] R. N. Euwema, D. J. Stukel, T. C. Collins, J. S. DeWitt, and D. G. Shankland, Phys. Rev. **178**, 1419 (1969).

[61] D. D. Koelling and J. H. Wood, J. Comput. Phys. **67**, 253 (1986).

[62] G. K. H. Madsen and D. J. Singh, Comput. Phys. Commun. **175**, 67 (2006).

[63] R. Del Sole and R. Girlanda, Phys. Rev. B **48**, 11789 (1993).

[64] P. E. Blöchl, O. Jepsen, and O. K. Andersen, Phys. Rev. B **49**, 16223 (1994).

[65] T. Sohier, D. Campi, N. Marzari, and M. Gibertini, Phys. Rev. Mater. **2**, 114010 (2018).

[66] T.-H. Liu, J. Zhou, B. Liao, D. J. Singh, and G. Chen, Phys. Rev. B **95**, 075206 (2017).

[67] D. Kammerlander, S. Botti, M. A. L. Marques, A. Marini, and C. Attaccalite, Phys. Rev. B **86**, 125203 (2012).

[68] Y. Gillet, M. Giantomassi, and X. Gonze, Comput. Phys. Commun. **203**, 83 (2016).

[69] M. Fiorentini and N. Bonini, Phys. Rev. B **94**, 085204 (2016).

[70] N. Troullier and J. L. Martins, Phys. Rev. B **43**, 1993 (1991).

[71] J. P. Perdew and Y. Wang, Phys. Rev. B **45**, 13244 (1992).

[72] D. M. Ceperley and B. J. Alder, Phys. Rev. Lett. **45**, 566 (1980).

[73] See Supplemental Material at http://link.aps.org/supplemental/10.1103/PhysRevB.102.094308 for more information about computational details and results, which includes Refs. [83–88].

[74] M. Giantomassi *et al.*, ABIPY project, https://github.com/abinit/abipy.

[75] G. Hautier, A. Miglio, G. Ceder, G. M. Rignanese, and X. Gonze, Nat. Commun. **4**, 2292 (2013).

[76] A. Bhatia, G. Hautier, T. Nilgianskul, A. Miglio, J. Sun, H. J. Kim, K. H. Kim, S. Chen, G. M. Rignanese, X. Gonze, and J. Suntivich, Chem. Mater. **28**, 30 (2016).

[77] F. Ricci, W. Chen, U. Aydemir, G. J. Snyder, G.-M. Rignanese, A. Jain, and G. Hautier, Sci. Data **4**, 170085 (2017).

[78] M. Darnon, R. Varache, M. Descazeaux, T. Quinci, M. Martin, T. Baron, and D. Muñoz, AIP Conf. Proc. **1679**, 040003 (2015).

[79] X. Gonze, Phys. Rev. B **55**, 10337 (1997).

[80] X. Gonze, P. Ghosez, and R. W. Godby, Phys. Rev. Lett. **74**, 4035 (1995).

[81] G. F. Bassani and G. P. Parravicini, *Electronic States and Optical Transitions in Solids*, 1st ed. (Pergamon Press, Oxford, New York, 1975).

[82] M. S. Hybertsen and S. G. Louie, Phys. Rev. B **35**, 5585 (1987).

[83] G. Petretto, S. Dwaraknath, H. P. C. Miranda, D. Winston, M. Giantomassi, M. J. Van Setten, X. Gonze, K. A. Persson, G. Hautier, and G. M. Rignanese, Sci. Data **5**, 180065 (2018).

[84] D. R. Hamann, Phys. Rev. B **88**, 085117 (2013).

[85] A. Damle and L. Lin, Multiscale Model. Simul. **16**, 1392 (2018).

[86] W. E. Pickett, Comput. Phys. Rep. **9**, 115 (1989).

[87] S. Calnan and A. N. Tiwari, Thin Solid Films **518**, 1839 (2010).

[88] I.-T. Lu, J.-J. Zhou, and M. Bernardi, Phys. Rev. Mater. **3**, 033804 (2019).

[89] V. A. Jhalani, J.-J. Zhou, J. Park, C. E. Dreyer, and M. Bernardi, Phys. Rev. Lett. **125**, 136602 (2020).

[90] J. Park, J.-J. Zhou, V. A. Jhalani, C. E. Dreyer, and M. Bernardi, Phys. Rev. B **102**, 125203 (2020).